

Rouse model with fluctuating internal friction

R. Kailasham,^{1,2,3} Rajarshi Chakrabarti,^{2, a)} and J. Ravi Prakash^{3, b)}

¹⁾ IITB-Monash Research Academy, Indian Institute of Technology Bombay, Mumbai, Maharashtra - 400076, India

²⁾ Department of Chemistry, Indian Institute of Technology Bombay, Mumbai, Maharashtra - 400076, India

³⁾ Department of Chemical Engineering, Monash University, Melbourne, VIC 3800, Australia

A coarse-grained bead-spring-dashpot chain model with the dashpots representing the presence of internal friction, is solved exactly numerically, for the case of chains with more than two beads. Using a decoupling procedure to remove the explicit coupling of a bead's velocity with that of its nearest neighbors, the governing set of stochastic differential equations are solved with Brownian dynamics simulations to obtain material functions in oscillatory and steady simple shear flow. Simulation results for the real and imaginary components of the complex viscosity have been compared with the results of previously derived semi-analytical approximations, and the difference in the predictions are seen to diminish with an increase in the number of beads in the chain. The inclusion of internal friction results in a non-monotonous variation of the viscosity with shear rate, with the occurrence of continuous shear-thickening following an initial shear-thinning regime. The onset of shear-thickening in the first normal stress difference coefficient is pushed to lower shear rates with an increase in the internal friction parameter.

I. INTRODUCTION

The presence of an additional mode of dissipation in polymer molecules arising from intramolecular interactions, denoted as internal friction or internal viscosity¹⁻⁷, has been invoked to reconcile the high values of dissipated work observed in force spectroscopic measurements on single molecules⁸⁻¹¹, the steepness of the probability distribution of polymer extensions in coil-stretch transitions observed in turbulent flow¹², and the dampened reconfiguration kinetics of biopolymers¹³⁻²⁵. The discontinuous jump in the stress in polymer solutions upon the inception or cessation of flow^{26,27} has also been attributed to internal friction. Given its wide-ranging impact, a careful investigation of the consequences of the presence of internal friction is essential. As shown in Fig. 1, the bead-spring-chain model^{28,29}, widely used to describe the dynamics of flexible polymer chains, has been modified to include a dashpot in parallel with each spring to account for internal friction effects^{2,28,30}. The dashpot provides a restoring force proportional to the relative velocity between adjacent beads, and acts along the connector vector joining these beads. The machinery for the solution of coarse-grained polymer models through Brownian dynamics (BD) simulations is well-established^{28,29}: the equation of motion for the connector vector velocities is combined with an equation of continuity in probability space to obtain a Fokker-Planck equation for the system, and the equivalent stochastic differential equation is integrated numerically. The inclusion of internal viscosity, however, results in a coupling of connector vector velocities and precludes a trivial application of the usual procedure for all but the simplest case of a dumbbell. By expanding the scope of an existing methodology for velocity-decoupling⁵, the exact set of governing stochastic differential equations for a bead-spring-dashpot chain

with N_b beads, and its numerical solution using BD simulations is presented here. The thermodynamically consistent³¹ stress tensor expression for this model is derived, and material functions in simple shear and oscillatory shear flows have been calculated.

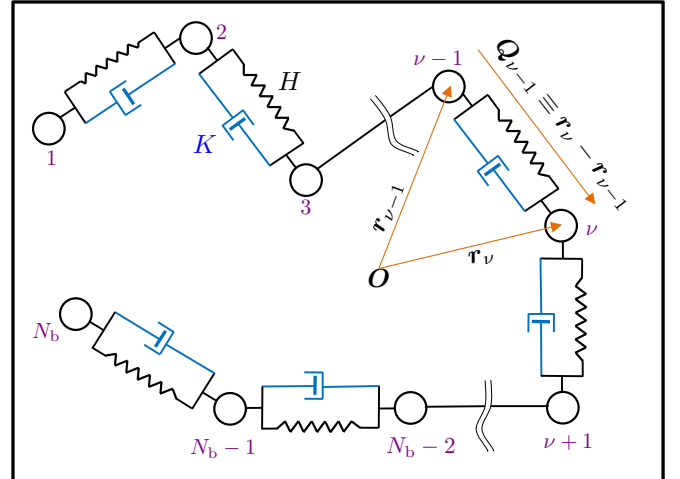


FIG. 1. Representation of a polymer chain as a sequence of beads connected by spring-dashpots. The Hookean spring constant associated with each spring is H , and the damping coefficient of each dashpot is K .

It is instructive to first briefly survey the methods employed in the past, before turning our attention to the solution proposed in the present work. Booij and van Wiechen² used perturbation analysis to expand the configurational distribution function of a Hookean spring-dashpot in terms of the internal friction parameter, $\varphi = K/\zeta$, which is the ratio of the dashpot's damping coefficient, K , to the bead friction coefficient, ζ , and predicted optical and rheological properties in the presence of steady shear flow. On the other hand, Williams and coworkers offered a semi-analytical approximate solution for the stress-jump⁵ of bead-spring-dashpot-chains with

^{a)} Electronic mail: rajarshi@chem.iitb.ac.in

^{b)} Electronic mail: ravi.jagadeeshan@monash.edu

an arbitrary number of beads, using a decoupling procedure which is discussed at length later in this paper. They also obtained predictions for the complex viscosity of such chains by writing the configurational distribution function as a series expansion in strain⁶. While the approach of Booij and van Wiechen² is restricted to small values of the internal friction parameter, the solutions proposed by Williams and coworkers^{5,6} are applicable only in the linear viscoelastic regime. The transient variation and steady-state values of viscometric functions of bead-spring-dashpot chains with arbitrary chain-length in shear flow have been predicted^{32,33} using the linearized rotational velocity^{34–36} (LRV) approximation for the internal viscosity force. The LRV approximation, however, was shown to be incorrect^{2,5,6} and its use was subsequently discarded. For the simplest case of a single-mode dumbbell-dashpot, it is straightforward to formulate the governing Fokker-Planck equation and obtain its equivalent stochastic differential equation. Both linear viscoelastic properties^{37,38} and viscometric functions in steady-shear flow^{38,39} have been calculated for this model using Brownian dynamics (BD) simulations, for arbitrary values of the internal friction parameter. The single-mode spring-dashpot model has also been solved using a Gaussian approximation for the distribution function^{40,41}. Upon comparison against exact BD simulation results, it was found that the Gaussian approximation (GA) offers accurate predictions of linear viscoelastic properties, but is unable to predict the shear-thickening of viscosity^{37,38} predicted by the exact model. Furthermore, the predictions for the stress jump in the start up of shear flow, obtained from BD simulations on the exact model, the Gaussian approximation, and the semi-analytical treatment of Manke and Williams agree with one another³⁷.

Fixman⁴² has shown that the effects of bond length and bond angle constraints in stiff polymer models may be sufficiently mimicked by a Rouse/Zimm-like chain with internal friction. A preaveraged form of the internal friction force was chosen for analytical tractability, and this simplified model yields predictions for equilibrium and linear viscoelastic properties, such as the bond-vector correlations and storage and loss moduli, that are in reasonable agreement with that of stiff polymer chains. McLeish and coworkers developed the Rouse model with internal friction⁴³ (RIF), wherein the standard continuum Rouse model is modified to include a rate-dependent dissipative force that resists changes in the curvature of the space-curve representing the polymer molecule. An expression for the autocorrelation of the end-to-end vector of the chain, and a closed-form expression for the frequency response of the chain has been derived by them⁴³. The RIF model, and its variants^{19,20,44} which include excluded volume interactions and preaveraged hydrodynamic interactions, has been widely used to interpret the results of experiments and simulations on conformational transitions in biopolymers^{17,45,46}, where the polymers do not experience a flow profile. The RIF model represents

a preaveraged treatment of internal friction, while, in this work, we have developed an exact model which accounts for fluctuations in the internal friction force. To the best of our knowledge, an expression for the transient evolution of the mean-squared end-to-end vector of an RIF chain in flow is unknown, as are the viscometric functions. A thorough test of the accuracy of the preaveraging approximation, by comparing model predictions for observables at equilibrium and in flow, against exact BD simulations which account for fluctuations in internal friction, will be published as a separate study⁴⁷.

There currently exists no methodology that is able to predict both linear viscoelastic properties and viscometric functions in shear flow for bead-spring-dashpot chains with arbitrary number of beads and magnitude of internal friction parameter. We address this deficiency by solving the bead-spring-dashpot chain problem exactly. We compare BD simulation results for the stress jump and complex viscosity against approximate analytical predictions given in Ref. 5 and Ref. 6, respectively, and present steady-state results for viscometric functions in simple shear flow for the general case of $N_b > 2$, for the first time.

A crucial step in our methodology is the decoupling of the connector vector velocities of neighboring beads. Stripping away all physical detail, the decoupling problem may be stated as follows: given a “generating equation” for some \mathcal{S}_j which is of the form

$$\mathcal{S}_j = d_{j-1}\mathcal{S}_{j-1} + e_{j+1}\mathcal{S}_{j+1} + \xi(X_1, X_2, \dots, X_N) \quad (1)$$

where $j \in [1, N]$, and the X_i do not depend on the \mathcal{S}_j , with $\{\xi, d_j, e_j\}$ being some arbitrary functions of the X_i , is it possible to write an expression for \mathcal{S}_j solely in terms of the X_i that does not explicitly depend on any other \mathcal{S}_i ? Manke and Williams⁵ have proposed a three-step procedure for the solution of this problem. As the first step, the equation for \mathcal{S}_j is successively substituted into \mathcal{S}_{j+1} , starting from $j = 1$. At the end of this forward substitution step, an equation for \mathcal{S}_j is obtained that only depends explicitly on \mathcal{S}_{j+1} and X_i with $1 \leq i \leq j$. The second step is a backward substitution, where the equation for \mathcal{S}_j is successively substituted into \mathcal{S}_{j-1} , starting from $j = N$. This results in an expression for \mathcal{S}_j that only depends explicitly on \mathcal{S}_{j-1} and X_i with $j \leq i \leq N$. Finally, upon combining the results from the forward and backward substitution procedures, the decoupling procedure is completed, resulting in $\mathcal{S}_j = \mathcal{A}_j \xi(X_1, X_2, \dots, X_N)$ where \mathcal{A}_j is defined recursively in terms of d and e . While the decoupling methodology developed by Manke and Williams has been adopted in the present work, we differ significantly in the generating equation which is subjected to the decoupling procedure. A detailed discussion highlighting the differences is given in Sec. II. A schematic representation of the decoupling methodology is displayed in Fig. 2.

The rest of the paper is structured as follows. Sec. II describes the bead-spring-dashpot chain model for a polymer, presents the governing stochastic differential

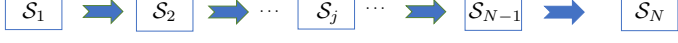
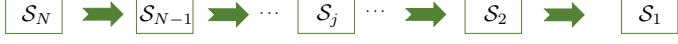
Decoupling Methodology	
Given $\mathcal{S}_j = d_{j-1}\mathcal{S}_{j-1} + e_{j+1}\mathcal{S}_{j+1} + \xi$, the following procedure leads to an expression for \mathcal{S}_j that does not depend explicitly on any other \mathcal{S}_i	
Step	Output
(1) Forward Substitution 	$\mathcal{S}_j \equiv f(\mathcal{S}_{j+1}, \xi)$
(2) Backward Substitution 	$\mathcal{S}_j \equiv g(\mathcal{S}_{j-1}, \xi)$
(3) Combine expressions from (1) and (2) to get decoupled expression for \mathcal{S}_j	$\mathcal{S}_j \equiv \mathcal{A}_j \xi$ $\mathcal{A}_j \equiv \hat{h}(\{d, e\})$

FIG. 2. Schematic of three-step decoupling methodology introduced in Manke and Williams⁵.

equations and the stress tensor expression, and contains simulation details pertaining to the numerical integration of the governing equations. Sec. III, which is a compilation of our results and the relevant discussion, is divided into three sections; Sec. III A deals with code validation, Sec. III B presents results for the complex viscosity calculated from oscillatory shear flow simulations, and Sec. III C contains results for steady shear viscometric functions. We conclude in Sec. IV. Appendix A contains the detailed steps showing the implementation of the decoupling algorithm represented in Fig. 2, and the derivation of the governing Fokker-Planck equation for the system.

As described later in detail, the governing stochastic differential equation and the stress tensor expression require the evaluation of a divergence term which does not appear in conventional bead-spring-chain models. The Supplementary Material outlines a procedure for evaluating these terms analytically. A brief comparison of the simulation time scaling of models with internal friction, as function of the number of beads in the chain, is also included in the Supplementary Material.

II. GOVERNING EQUATION AND SIMULATION DETAILS

We consider N_b massless beads, each of radius a , joined by $N \equiv (N_b - 1)$ springs, each of Hookean spring constant H , with a dashpot of damping coefficient K in parallel with each spring, as shown in Fig. 1. The position of the i^{th} bead is denoted as \mathbf{r}_i , and the connector vector joining adjacent beads is represented as $\mathbf{Q}_i \equiv \mathbf{r}_{i+1} - \mathbf{r}_i$. As will be seen shortly, in the absence of hydrodynamic interactions (HI), the inclusion of internal viscosity (IV) results in an explicit coupling of the connector vector velocities between nearest neighbors, and these velocities may be decoupled using the procedure suggested

by Manke and Williams⁵. The simultaneous inclusion of fluctuating hydrodynamic interactions and internal viscosity, however, results in a one-to-all coupling of the connector vector velocities, which renders the problem intractable using the Manke and Williams approach⁵. It is noted, however, that in dumbbell models with internal viscosity, hydrodynamic interactions significantly magnify the stress jump and perceptibly affect the transient viscometric functions³⁸. Coarse-grained polymer models which incorporate both fluctuating hydrodynamic interactions and internal viscosity are currently unsolved for the $N_b > 2$ case. In this work, we restrict our attention to freely-draining bead-spring-dashpot chains.

The chain, as shown in Fig. 1, is suspended in a Newtonian solvent of viscosity η_s where the velocity \mathbf{v}_f at any location \mathbf{r}_f in the fluid is given by $\mathbf{v}_f(\mathbf{r}_f, t) \equiv \mathbf{v}_0 + \boldsymbol{\kappa}(t) \cdot \mathbf{r}_f$, where \mathbf{v}_0 is a constant vector, and the transpose of the velocity gradient tensor is denoted as $\boldsymbol{\kappa} \equiv (\nabla \mathbf{v}_f)^T$. The chain is assumed to have completely equilibrated in momentum space, and its normalized configurational distribution function at any time t is specified as $\Psi \equiv \Psi(\mathbf{r}_1, \mathbf{r}_2, \dots, \mathbf{r}_{N_b}, t) = (1/\mathcal{Z}) \exp[-\phi/k_B T]$, where ϕ denotes the intramolecular potential energy stored in the springs joining the beads, k_B is Boltzmann's constant, T the absolute temperature, and $\mathcal{Z} = \int \exp[-\phi/k_B T] d\mathbf{Q}_1 d\mathbf{Q}_2 \dots d\mathbf{Q}_N$. The spring force in the k^{th} connector vector is denoted as $\mathbf{F}_k^s = \partial\phi/\partial\mathbf{Q}_k$, with $\mathbf{F}_k^s = H\mathbf{Q}_k$ for a Hookean spring. The expression for the internal viscosity force, \mathbf{F}_k^{IV} , in the k^{th} connector vector may be written as $\mathbf{F}_k^{\text{IV}} = K(\mathbf{Q}_k \mathbf{Q}_k / Q_k^2) \cdot [\dot{\mathbf{Q}}_k]$, where $[\dots]$ denotes an average over momentum-space. Within the framework of polymer kinetic theory²⁸, the Fokker-Planck equation for the configurational distribution function is obtained by combining a force-balance on the beads (or connector vectors) with a continuity equation in probability space. The force-balance mandates that the sum of: (i) the internal friction force due

to the dashpot, (ii) the restoring force from the Hookean spring, (iii) the random Brownian force arising from collisions with solvent molecules, and (iv) the hydrodynamic force which represents the solvent's resistance to the motion of the bead, equals zero. It is convenient to work with connector vectors, rather than bead positions, for models with internal friction, and the following equation is obtained for the momentum-averaged velocity of the k^{th} connector vector

$$\begin{aligned} \llbracket \dot{\mathbf{Q}}_k \rrbracket = & \boldsymbol{\kappa} \cdot \mathbf{Q}_k - \frac{1}{\zeta} \sum_l \mathbf{A}_{kl} \cdot \left(\underline{k_B T \frac{\partial \ln \Psi}{\partial \mathbf{Q}_l}} + \underline{\frac{\partial \phi}{\partial \mathbf{Q}_l}} \right. \\ & \left. + K \frac{\mathbf{Q}_l \mathbf{Q}_l}{Q_l^2} \cdot \llbracket \dot{\mathbf{Q}}_l \rrbracket \right) \end{aligned} \quad (2)$$

where $\zeta := 6\pi\eta_s a$ is the monomeric friction coefficient, and $\mathbf{A}_{kl} = A_{kl}\boldsymbol{\delta}$ where A_{kl} are the elements of the Rouse matrix, given by

$$A_{kl} = \begin{cases} 2; & k = l \\ -1; & |k - l| = 1 \\ 0; & \text{otherwise} \end{cases} \quad (3)$$

and the solid and dashed underlined terms on the RHS

of Eq. (2) represent the Brownian and spring force contributions, respectively. Since Manke and Williams⁵ were concerned only with the evaluation of the stress-jump, which occurs instantaneously upon the inception of flow, they assumed that the configurational distribution function may be reasonably approximated by its equilibrium value. Since the Brownian and spring forces exactly balance each other at equilibrium, i.e., $k_B T (\partial \ln \Psi_{\text{eq}} / \partial \mathbf{Q}_l) + (\partial \phi / \partial \mathbf{Q}_l) = 0$, Manke and Williams⁵ ignore both these forces in their equation of motion. Here, however, we aim to find the exact governing equation that is valid both near and far away from equilibrium, and have consequently retained both the underlined terms in the force-balance equation.

As seen from Eq. (2), there is an explicit coupling between the velocity of the k^{th} connector vector and its nearest neighbors which precludes a straightforward substitution into the equation of continuity for the configurational distribution function. This velocity-coupling may be removed by applying the decoupling scheme described in Fig. 2, to obtain the governing Fokker-Planck equation for the system, as shown in Appendix A. Using $l_H \equiv \sqrt{k_B T / H}$ and $\lambda_H \equiv \zeta / 4H$ as the length- and time-scales, respectively, and denoting dimensionless variables with an asterisk as superscript, the dimensionless form of the Fokker-Planck equation is given as

$$\begin{aligned} \frac{\partial \psi^*}{\partial t^*} = & - \sum_{j=1}^N \frac{\partial}{\partial \mathbf{Q}_j^*} \cdot \left\{ \left[\boldsymbol{\kappa}^* \cdot \mathbf{Q}_j^* - \left(\frac{\varphi}{1+2\varphi} \right) \sum_{k=1}^N \mathbf{U}_{jk} \cdot (\boldsymbol{\kappa}^* \cdot \mathbf{Q}_k^*) - \frac{1}{4} \sum_{k=1}^N \hat{\mathbf{A}}_{jk} \cdot \mathbf{F}_k^{*s} \right. \right. \\ & \left. \left. - \frac{1}{4} \left(\frac{\varphi}{1+2\varphi} \right) \sum_{k=1}^N \frac{\partial}{\partial \mathbf{Q}_k^*} \cdot \mathbf{V}_{jk}^T \right] \psi^* \right\} + \frac{1}{4} \sum_{j,k=1}^N \frac{\partial}{\partial \mathbf{Q}_j^*} \frac{\partial}{\partial \mathbf{Q}_k^*} : [\hat{\mathbf{A}}_{jk}^T \psi^*] \end{aligned} \quad (4)$$

where the definitions of the dimensionless tensors, \mathbf{U}_{jk} , \mathbf{V}_{jk} , and $\hat{\mathbf{A}}_{jk}$, are provided in Eqs. (A23) and (A32) of Appendix A. In the absence of internal friction, both \mathbf{U}_{jk} and \mathbf{V}_{jk} reduce to $\mathbf{0}$, and $\hat{\mathbf{A}}_{jk}$ becomes the Rouse matrix. In order to simplify the notation, it is convenient to rewrite the Fokker-Planck equation in terms of collective coordinates. We define

$$\begin{aligned} \tilde{\mathbf{Q}}^* & \equiv [\mathbf{Q}_1^*, \mathbf{Q}_2^*, \dots, \mathbf{Q}_N^*] \\ & \equiv [Q_1^{*1}, Q_1^{*2}, Q_1^{*3}, Q_2^{*1}, Q_2^{*2}, \dots, Q_N^{*3}] \end{aligned}$$

and write $\tilde{Q}_i^* = Q_k^{*\beta}$, where $k = 1, 2, \dots, N$ and $\beta =$

1, 2, 3 (represent Cartesian components in the x, y, z directions, respectively), with i related to k and β as $i = 3(k-1) + \beta$. Similarly, $\tilde{\mathbf{F}}^{*s} \equiv [\mathbf{F}_1^{*s}, \mathbf{F}_2^{*s}, \dots, \mathbf{F}_N^{*s}]$, and $\tilde{\mathbf{v}}^* \equiv [\hat{\mathbf{v}}_1^*, \hat{\mathbf{v}}_2^*, \dots, \hat{\mathbf{v}}_N^*]$, with $\hat{\mathbf{v}}_j^* = \sum_{k=1}^N (\partial / \partial \mathbf{Q}_k^*) \cdot \mathbf{V}_{jk}^T$. The diffusion matrix \mathcal{D} of size $N \times N$ is defined, whose elements are the tensors $\hat{\mathbf{A}}_{jk}$. The block matrix \mathcal{K}^* is defined such that its diagonal elements are given by the 3×3 matrix $\boldsymbol{\kappa}^*$, and its off-diagonal blocks are $\mathbf{0}$. Lastly, the block matrix \mathcal{U} consists of the tensors \mathbf{U}_{jk} . In terms of these collective variables, the stochastic differential equation equivalent to Eq. (4), using Itô's interpretation²⁹, is given by

$$d\tilde{\mathbf{Q}}^* = \left[\boldsymbol{\kappa}^* \cdot \tilde{\mathbf{Q}}^* - \left(\frac{\varphi}{1+2\varphi} \right) \mathcal{U} \cdot (\boldsymbol{\kappa}^* \cdot \tilde{\mathbf{Q}}^*) - \frac{1}{4} \mathcal{D} \cdot \tilde{\mathbf{F}}^{*s} - \frac{1}{4} \left(\frac{\varphi}{1+2\varphi} \right) \tilde{\mathbf{v}}^* \right] dt^* + \frac{1}{\sqrt{2}} \mathcal{B} \cdot d\tilde{\mathbf{W}}^* \quad (5)$$

where $\tilde{\mathbf{W}}^*$ is a $3N$ -dimensional Wiener process, and $\mathbf{B} \cdot \mathbf{B}^T = \mathcal{D}$. The symmetricity and positive-definiteness of the diffusion matrix is established empirically in Section II F of the Supplementary Material. The square-root of the diffusion matrix is found using Cholesky decomposition⁴⁸. Equation (5) is solved numerically using a simple explicit Euler method, as follows

$$\begin{aligned} \tilde{\mathbf{Q}}^*(t_{n+1}) = & \tilde{\mathbf{Q}}_n^* + \left[\mathbf{\kappa}^*(t_n) \cdot \tilde{\mathbf{Q}}^*(t_n) - \left(\frac{\varphi}{1+2\varphi} \right) \mathbf{u}(t_n) \cdot \left(\mathbf{\kappa}^*(t_n) \cdot \tilde{\mathbf{Q}}^*(t_n) \right) - \frac{1}{4} \mathcal{D}^*(t_n) \cdot \tilde{\mathbf{F}}^{*s}(t_n) \right. \\ & \left. - \left(\frac{1}{4} \right) \left(\frac{\varphi}{1+2\varphi} \right) \tilde{\mathbf{v}}^*(t_n) \right] \Delta t_n + \frac{1}{\sqrt{2}} \Delta \tilde{\mathbf{S}}_n^* \end{aligned} \quad (6)$$

where $\Delta \tilde{\mathbf{S}}_n^* = \mathbf{B} \cdot \Delta \tilde{\mathbf{W}}_n^*$.

In order to relate the time-evolution of the connector vectors to macroscopically observable rheological properties, it is necessary to specify an appropriate stress tensor expression for the model discussed above. The formal, thermodynamically consistent stress tensor expression for free-draining models with internal friction may be obtained using the Giesekus expression³¹, as follows

$$\tau_p = \frac{n_p \zeta}{2} \left\langle \sum_{j=1}^N \sum_{k=1}^N \mathcal{C}_{jk} \mathbf{Q}_j \mathbf{Q}_k \right\rangle_{(1)} = \frac{n_p \zeta}{2} \left[\frac{d}{dt} \left\langle \sum_{j,k} \mathcal{C}_{jk} \mathbf{Q}_j \mathbf{Q}_k \right\rangle - \mathbf{\kappa} \cdot \left\langle \sum_{j,k} \mathcal{C}_{jk} \mathbf{Q}_j \mathbf{Q}_k \right\rangle - \left\langle \sum_{j,k} \mathcal{C}_{jk} \mathbf{Q}_j \mathbf{Q}_k \right\rangle \cdot \mathbf{\kappa}^T \right] \quad (7)$$

where \mathcal{C}_{jk} is the Kramers matrix²⁸. Upon simplification,

$$\tau_p = n_p k_B T (N_b - 1) \delta - n_p \left\langle \sum_{k=1}^{N_b-1} \mathbf{Q}_k \mathbf{F}_k^c \right\rangle \quad (8)$$

which is formally similar to the Kramers expression²⁸, except that the force in the connector vector, \mathbf{F}_k^c , is redefined to include contributions from both the spring and the dashpot (also noted in Refs. [31,39,49] for Hookean dumbbells with IV), as follows,

$$\mathbf{F}_k^c = \mathbf{F}_k^s + K C_k \mathbf{Q}_k \quad (9)$$

where $C_k = (\mathbf{Q}_k \cdot \dot{\mathbf{Q}}_k) / Q_k^2$. Plugging Eq. (9) into Eq. (8) and using the closed-form expression for C_k as given by Eq. (A20), the dimensionless stress tensor expression is obtained as

$$\begin{aligned} \frac{\tau_p}{n_p k_B T} = & (N_b - 1) \delta - \left[\left\langle \sum_k \mathbf{Q}_k^* \mathbf{F}_k^{*s} \right\rangle - \frac{1}{2} \left(\frac{\epsilon}{1+\epsilon} \right) \left\langle \sum_{k,l} (\mathbf{Q}_k^* \mathbf{F}_l^{*s}) \cdot \boldsymbol{\mu}_{kl}^T \right\rangle \right] - \frac{1}{2} \left(\frac{\epsilon}{1+\epsilon} \right) \left[\left\langle \sum_k \boldsymbol{\mu}_{kk}^T \right\rangle \right. \\ & \left. + \left\langle \sum_{k,l} \mathbf{Q}_k^* \frac{\partial}{\partial \mathbf{Q}_l^*} \cdot \boldsymbol{\mu}_{kl}^T \right\rangle \right] - \left(\frac{2\epsilon}{1+\epsilon} \right) \mathbf{\kappa}^* : \left\langle \sum_{k,l} \frac{\chi_l^{(k)} \mathbf{Q}_l^* \mathbf{Q}_l^* \mathbf{Q}_k^* \mathbf{Q}_k^*}{Q_l^* Q_k^*} \right\rangle \end{aligned} \quad (10)$$

where $\epsilon = 2\varphi$, and the definitions of $\boldsymbol{\mu}_{kl}$ and $\chi_l^{(k)}$ are provided in Eqs. (A23) and (A25) of Appendix A.

The bead-spring-dashpot chain is subjected to steady simple shear flow and small amplitude oscillatory shear flow. The flow tensor, $\mathbf{\kappa}$, for simple shear flow has the following form

$$\mathbf{\kappa} \equiv \mathbf{\kappa}^* \lambda_H^{-1} = \dot{\gamma} \begin{pmatrix} 0 & 1 & 0 \\ 0 & 0 & 0 \\ 0 & 0 & 0 \end{pmatrix} \quad (11)$$

and is characterized by the following viscometric func-

tions

$$\begin{aligned} \eta_p &= -\frac{\tau_{p,xy}}{\dot{\gamma}} \\ \Psi_1 &= -\left[\frac{\tau_{p,xx} - \tau_{p,yy}}{\dot{\gamma}^2} \right] \\ \Psi_2 &= -\left[\frac{\tau_{p,yy} - \tau_{p,zz}}{\dot{\gamma}^2} \right] \end{aligned} \quad (12)$$

where $\tau_{p,xy}$ refers to the xy element of the stress tensor,

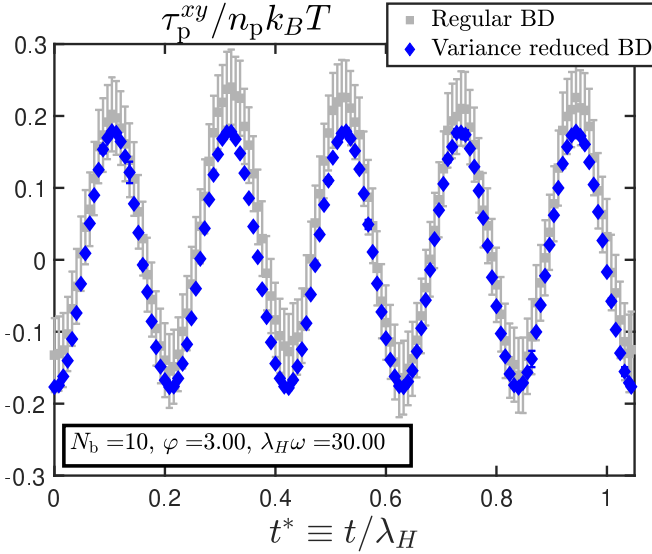


FIG. 3. Illustration of the efficacy of variance reduction for a ten-bead chain with internal friction in small amplitude oscillatory shear flow.

and η_p , Ψ_1 , and Ψ_2 denote the shear viscosity, the first normal stress difference coefficient, and the second normal stress difference coefficient, respectively. For small-amplitude oscillatory shear flow, we have

$$\boldsymbol{\kappa} = \dot{\gamma}_0 \cos(\omega t) \begin{pmatrix} 0 & 1 & 0 \\ 0 & 0 & 0 \\ 0 & 0 & 0 \end{pmatrix} \quad (13)$$

The material functions relevant to this flow profile, $\eta'(\omega)$ and $\eta''(\omega)$, are given by

$$-\tau_{p,xy} = \eta'(\omega)\dot{\gamma}_0 \cos(\omega t) + \eta''(\omega)\dot{\gamma}_0 \sin(\omega t) \quad (14)$$

Variance reduction^{29,50} has been used in the evaluation of steady-shear viscometric functions at low shear rates ($\lambda_H\dot{\gamma} < 1.0$), and for the calculation of oscillatory shear material functions at all frequencies reported in this work. In Fig. 3, the effectiveness of variance reduction in oscillatory shear flow has been illustrated by comparison against data obtained from control simulations without variance reduction, for the same ensemble size of 10^4 trajectories and a step-size of $\Delta t^* = 10^{-3}$.

Where appropriate, the viscometric functions have either been scaled by their respective Rouse chain values, η^R and Ψ_1^R , in steady shear flow, given as²⁸

$$\eta^R = n_p k_B T \lambda_H \left[\frac{N_b^2 - 1}{3} \right] \quad (15)$$

$$\Psi_1^R = 2n_p k_B T \lambda_H^2 \left[\frac{(N_b^2 - 1)(2N_b^2 + 7)}{45} \right] \quad (16)$$

or by the Rouse values of the real and imaginary portions

of the complex viscosity given by²⁸

$$(\eta')^R = n_p k_B T \sum_{j=1}^N \frac{\lambda_j}{1 + (\lambda_j \omega)^2} \quad (17)$$

$$(\eta'')^R = n_p k_B T \sum_{j=1}^N \frac{\lambda_j^2 \omega}{1 + (\lambda_j \omega)^2} \quad (18)$$

where $\lambda_j = 2\lambda_H/a_j$, and $a_j = 4\sin^2[j\pi/2N_b]$ are the eigenvalues of the Rouse matrix. Note that the dynamic viscosity, η' , has the solvent viscosity contribution subtracted off and the convention is followed throughout this paper. Shear rates and angular frequencies are scaled using $\lambda_p \equiv (\eta^R/n_p k_B T)$, which is the characteristic relaxation time defined using the Rouse viscosity.

The underlined terms in Eqs. (6) and (10) may be calculated by two routes: analytically, using recursive functions as explained in Sec. II of the Supplementary Material, or they can be calculated numerically. The connector vectors appearing in Eqs. (19)–(20) below are in their dimensionless form, with the asterisks omitted for the sake of clarity. The numerical route for the calculation of divergence is described below. Consider the general divergence,

$$\frac{\partial}{\partial Q_k} \cdot \mathbf{g}_{jk} = \sum_{\beta=1}^3 \sum_{\gamma=1}^3 \frac{\partial}{\partial Q_k^\beta} \left(\mathbf{g}_{jk}^{\beta\gamma} \right) \mathbf{e}_\gamma \quad (19)$$

where β and γ run over the three Cartesian indices, \mathbf{g}_{jk} is a configuration-dependent tensor, and \mathbf{e}_γ is a unit vector. The computation of the divergence requires the calculation of nine gradient terms, which are evaluated using the central-difference approximation. One such evaluation is shown here as an example:

$$\frac{\partial}{\partial Q_k^1} (\mathbf{g}_{jk}^{12}) = \frac{1}{2\Delta_1} \left[\mathbf{g}_{jk}^{12} (Q_k^1 + \Delta_1, Q_k^2, Q_k^3) - \mathbf{g}_{jk}^{12} (Q_k^1 - \Delta_1, Q_k^2, Q_k^3) \right] \quad (20)$$

where Δ_1 is the spatial discretization width along one Cartesian direction, representing the infinitesimal change in Q_k^1 . The error in the evaluation of the gradient using this approximation scales as $\mathcal{O}(\Delta_1^2)$. We have validated that the divergences calculated numerically agrees with that obtained using recursive functions, and have chosen the numerical route in view of its faster execution time that is largely invariant with chain length. In numerical computations, we set $\Delta_1 = \Delta_2 = \Delta_3 = \Delta_d = 10^{-5}$, unless noted otherwise.

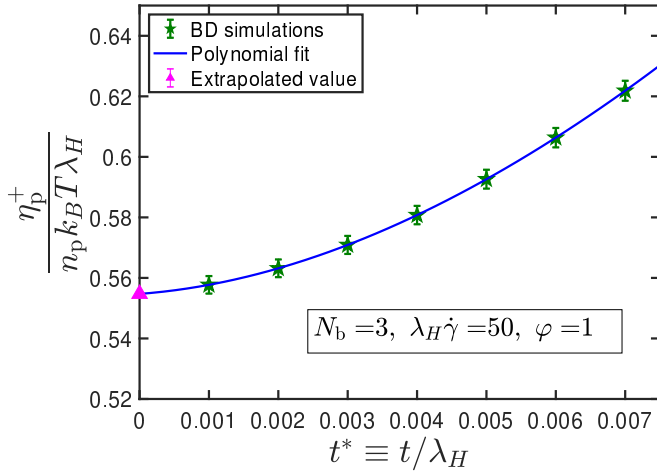


FIG. 4. Procedure for estimation of stress jump illustrated for a three-bead chain with $\varphi = 1.0$, subjected to steady-shear flow at $\lambda_H \dot{\gamma} = 50$. A fourth order polynomial is fit to the transient shear viscosity data, to obtain the extrapolated value at $t^* = 0.0$.

III. RESULTS

A. Code Validation

In Fig. 4, the methodology for the estimation of the shear stress jump from BD simulations is illustrated for a three-bead chain with an internal friction parameter of unity, subjected to a dimensionless shear rate of $\lambda_H \dot{\gamma} = 50$. The shear viscosity is recorded as a function of time, and a fourth order polynomial is fit through the data points, to obtain its extrapolated value at $t^* = 0$, which represents the stress-jump, as indicated by the triangle.

In Fig. 5, the stress-jump calculated for different chain lengths using the procedure described above is plotted as a function of the dimensionless shear rate. It is observed that the stress jump is independent of the shear rate, in agreement with the theoretically expected trend⁷. The horizontal lines in the figure represent the approximate analytical values for the stress jump evaluated by Manke and Williams⁵, and very good agreement is observed between the values estimated using the two approaches.

In Fig. 6 (a), the stress jump evaluated from BD simulations for two different values of the internal friction parameter is plotted as a function of the number of springs in the chain. The semi-analytical approximation of Manke and Williams⁵ is found to compare favourably against the exact simulation result. Furthermore, it is observed that the stress jump scales linearly with number of springs in the chain, with the slope of the line dependent on the internal friction parameter. It is instructive to first understand the two simplifying assumptions made in Manke and Williams⁵ before interpreting the data in Fig. 6 (b) where the percentage difference between the analytical and simulation results is plotted as a function of chain length at a fixed value of the internal friction

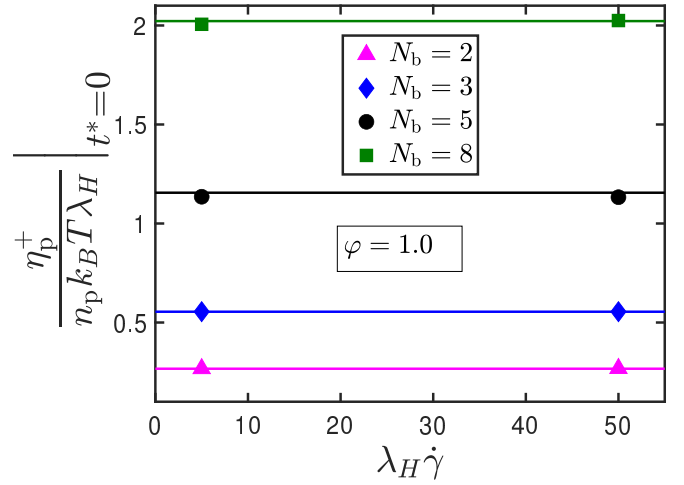


FIG. 5. Stress jump as a function of dimensionless shear rate for various chain lengths and a fixed internal friction parameter of $\varphi = 1.0$. Lines are approximate solutions by Manke and Williams⁵. Error bars are smaller than symbol size.

parameter. The first assumption is that the configurational distribution function at the inception of flow may be approximated by its equilibrium value, as mentioned in the discussion surrounding Eq. (A4). Secondly, it is assumed that the terminal connector vectors and interior connector vectors contribute equally towards the stress jump. This assumption is necessary only for chains with $N > 2$, because there is no distinction between a terminal and interior connector vector for a dumbbell ($N = 1$), and the two connector vectors for the $N = 2$ case are shown by Manke and Williams⁵, using the first assumption, to contribute identically to the total stress jump. It is anticipated that the second assumption would be most severely tested in chains with fewer number of springs, where the terminal springs represent a larger fraction of the overall chain, and becomes progressively better with an increase in the number of springs. The expected trend is clearly borne out by Fig. 6 (b), where the deviation between the exact simulation result and the analytical value first increases (beyond $N = 1$) and later decreases with the number of springs in the chain.

B. Complex viscosity from oscillatory shear flow

In Fig. 7, the material functions in oscillatory shear flow are plotted for a fixed value of the internal friction parameter, and varying number of beads in the chain. The exact BD simulation results, indicated by symbols, are compared against the approximate prediction given by Dasbach, Manke, and Williams⁶, shown as solid lines. Schieber⁴⁰ has obtained predictions for η' and η'' for Hookean dumbbells ($N_b = 2$) with internal viscosity, using a Gaussian approximation (GA), and these predictions have been shown using dash-dotted lines. The high-

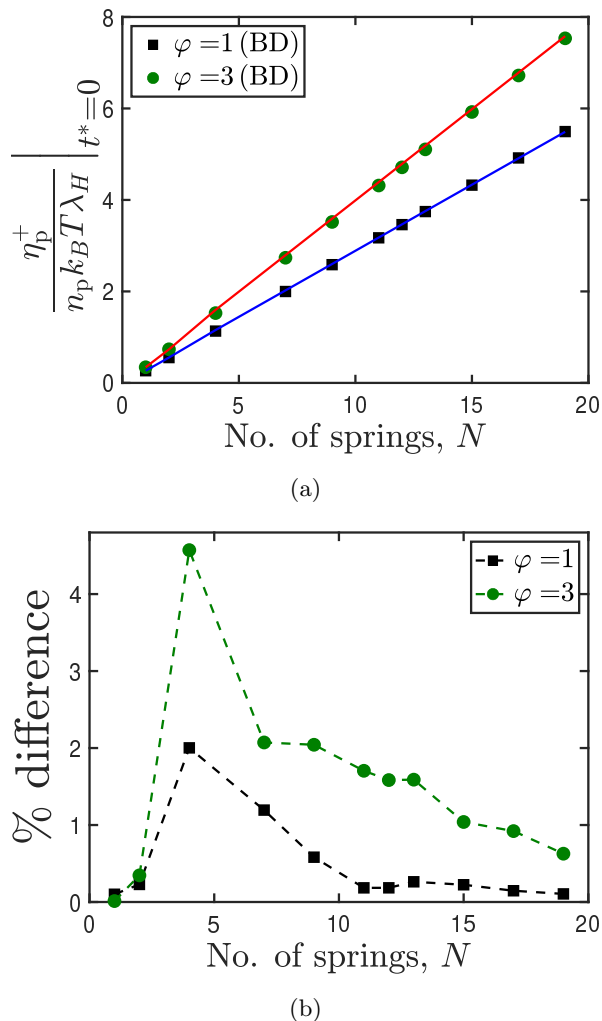


FIG. 6. (a) Comparison of stress jump obtained using extrapolation of BD simulation data, and approximate solutions by Manke and Williams⁵ indicated by solid lines. (b) Percentage difference between stress jump obtained using the two approaches, as a function of chain length. Dashed lines are drawn to guide the eye. Error bars are smaller than symbol size.

frequency-limiting value of η' obtained by GA agrees with that derived by Dasbach, Manke, and Williams⁶. Furthermore, while the functional form of η'' obtained by GA matches with the expression given by Dasbach, Manke, and Williams⁶, they differ in the sense that the GA predicts a φ -dependent rescaling of the frequency which is absent in the latter work.

As seen from Fig. 7 (a), the inclusion of internal friction into the Rouse model introduces a qualitative change in the variation of the dynamic viscosity, η' , with the appearance of a plateau in the high-frequency regime, in contrast to the Rouse model where $\eta' \rightarrow 0$ in the high-frequency limit. The numerical value of the plateau is equal to the stress jump, as seen from our simulations, which is in agreement with the theoretical prediction

of Gerhardt and Manke⁷. Since the stress jump scales linearly with the number of beads in the chain [Fig. 6 (a)], and the Rouse viscosity, η^R , scales as N^2 [Eq. (15)], the height of the high-frequency plateau decreases with an increase in the number of beads in the chain. The difference in the dynamic viscosity for the three different cases are less perceptible in the low frequency regime, where they are all seen to approach the respective Rouse viscosity. The GA prediction⁴⁰ is seen to perform marginally better than the Dasbach, Manke, and Williams⁶ prediction at low frequencies. With the increase in the number of beads, the Dasbach, Manke, and Williams⁶ approximation compares satisfactorily against BD simulation results.

In Fig. 7 (b), the dynamic viscosity for chains with internal friction is scaled by its corresponding values for a Rouse chain and plotted as a function of scaled frequency. It is seen that the departure from Rouse prediction is pushed to higher values of the scaled frequency with an increase in the number of beads. Furthermore, since models with internal friction predict a saturation of the dynamic viscosity at high frequencies, and since the Rouse model prediction in the high frequency regime decays asymptotically as $\sim \omega^{-2}$ [Eq. 17], the scaled dynamic viscosity is expected to vary as $\sim \omega^2$ at high frequencies. This scaling is observed for all three cases examined in Fig. 7 (b). The long-chain ($N_b = 100$) result predicted by the Dasbach, Manke, and Williams⁶ plotted on the same graph, further enunciates that for a fixed value of φ , the effect of internal friction decays with an increase in chain length.

A similar weakening of internal friction effects has also been predicted by the RIF model⁴³, where the relaxation time of a mode q is simply the sum of a mode-number-dependent Rouse contribution ($\tau_q^R \equiv \tau^R/q^2$), and an internal friction contribution (τ_{int}) that is independent of mode-number. Here, $\tau^R = (N_b^2 \zeta / \pi^2 H)$ is the Rouse relaxation time, and $\tau_{\text{int}} = K/H$ is a characteristic timescale defined on the basis of the damping coefficient of the dashpot. The relative magnitude of the two timescales is then

$$\frac{\tau_{\text{int}}}{\tau_q^R} = \left(\frac{\pi q}{N_b} \right)^2 \varphi \quad (21)$$

Two aspects are clear from the pre-averaged model predictions, for a fixed value of φ : Firstly, for a fixed chain length, the effects of internal friction are most pronounced at the higher mode numbers, i.e., at short time scales, and has the least impact on the global relaxation time, corresponding to the $q = 1$ case. This aspect is qualitatively evident from Fig. 7 (b): at low frequencies, where long wavelength motions (low mode numbers) are perturbed, the dynamic viscosity for chains with internal friction is indistinguishable from the Rouse value. At higher frequencies, where short wavelength motions (large mode numbers) are probed, a clear departure from the Rouse value is observed, and one could consider that the deviation occurs at some critical mode number for

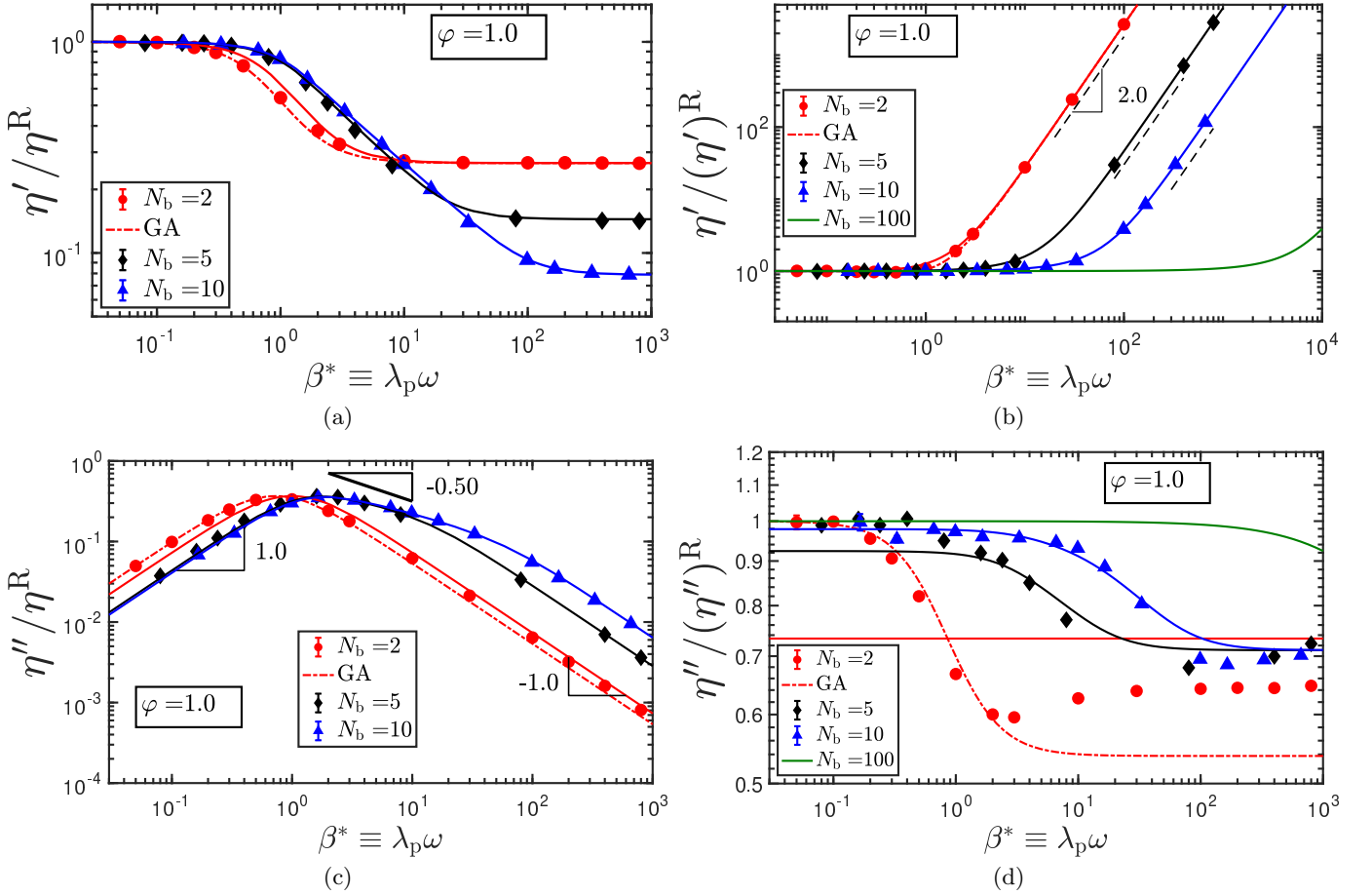


FIG. 7. Plots of the real (η') and imaginary components (η'') of the complex viscosity, as a function of the scaled frequency, for a fixed value of the internal friction parameter and three different values for the number of beads in the chain. The solid lines are approximate solutions given in Dasbach, Manke, and Williams⁶. The dash-dotted lines represent predictions obtained using the Gaussian approximation⁴⁰. Error bars are smaller than symbol size.

a given chain length. Secondly, for a given mode number, the effect of internal friction diminishes with an increase in the chain length. This trend is also evident from Fig. 7 (b), where it is observed that the onset of deviation from the Rouse prediction is pushed to higher frequencies with an increase in chain length. Hagen and coworkers^{16,51,52} predict, based on experimental reconfiguration time measurements on proteins, that the effect of internal friction is most easily discernible in short molecules that fold on microsecond-timescales, and could scarcely be detected in longer molecules whose folding times are in the millisecond range.

In Fig. 7 (c), the imaginary component of the complex viscosity, η'' , is normalized by the Rouse viscosity and plotted as a function of the scaled frequency. The Rouse scaling exponents at the low, intermediate and high frequency regimes are indicated in the figure. It is seen that inclusion of internal friction does not affect the Rouse scaling at low and high frequencies. In the intermediate frequency regime, a power law region appears with an increase in the number of beads, with an expo-

nent not exactly identical to the Rouse value. However, it is anticipated that the Rouse exponent in the intermediate frequency regime would be attained for chains with greater number of beads. As observed in the case of η' , the accuracy of the Dasbach, Manke, and Williams⁶ prediction is seen to improve with an increase in the number of beads. Notably, for the two-bead case, the GA prediction for η'' is closer to the BD results at low frequencies, but a slight deviation is observed at values of the scaled frequency, $\beta^* > 2$.

In Fig. 7 (d), η'' is normalized by its corresponding value for a Rouse chain and plotted as a function of frequency. At the coarsest level of discretization ($N_b = 2$), there is a striking, qualitative difference between the Dasbach, Manke, and Williams⁶ approximation and exact BD simulation results, in that the former predicts a frequency-independent response, while the latter exhibits a frequency-dependent variation which is also seen in models with higher number of beads. The GA prediction, however, captures the frequency dependence at the $N_b = 2$ level, but is unable to account for the slight in-

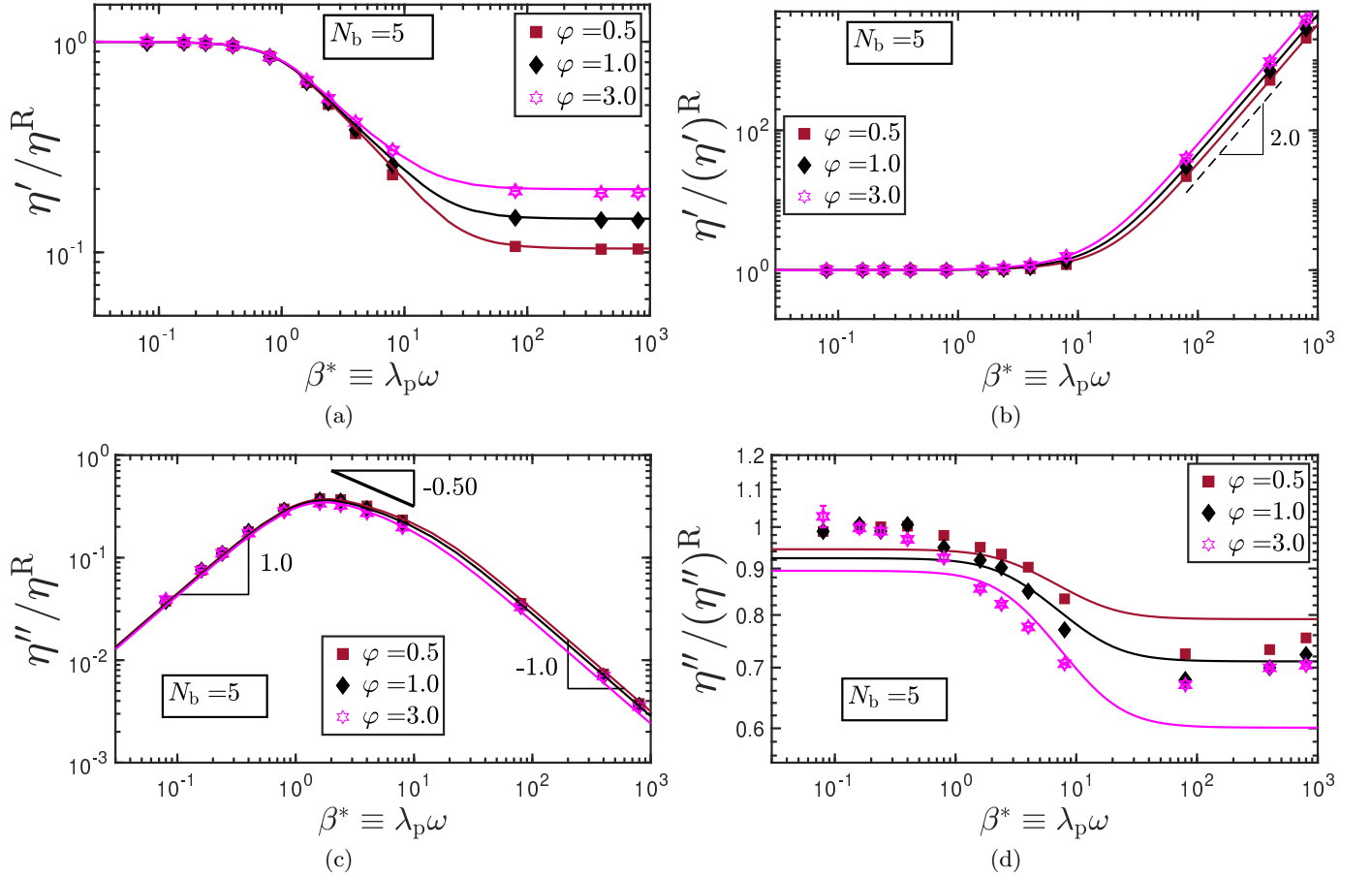


FIG. 8. Plots of the real (η') and imaginary components (η'') of the complex viscosity, as a function of the scaled frequency, for a fixed value of the internal friction parameter and three different values for the number of beads in the chain. The lines are approximate solutions given in Dasbach, Manke, and Williams⁶. Error bars are smaller than symbol size.

crease observed at $\beta^* > 2$, and underestimates the magnitude of the high-frequency plateau. Furthermore, the low-frequency plateau for all the three values of the chain lengths (N_b) simulated is seen to approach unity, which is also the value predicted by the Dasbach, Manke, and Williams⁶ approximation in the long-chain ($N_b = 100$) limit. Additionally, the onset of decrease in $\eta'' / (\eta'')^R$ is pushed to higher frequencies as the number of beads in the chain is increased.

In Fig. 8, the effect of the internal friction parameter on material functions in oscillatory shear flow is examined for a five-bead chain. The exact BD simulation results, indicated by symbols, are compared against the the approximate prediction given by Dasbach, Manke, and Williams⁶, shown as lines.

As seen from Fig. 8 (a), the height of the high-frequency plateau in the dynamic viscosity varies directly with the magnitude of the internal friction parameter. The low frequency, or long wavelength, response of the chain is unaffected by a variation in the internal friction parameter. In Fig. 8 (b), the dynamic viscosity normalized by its corresponding value for a Rouse chain and

plotted as a function of the scaled frequency. This quantity is seen to increase as the square of the frequency, for the same reasons elaborated in connection with Fig. 7 (b).

In Fig. 8 (c), the imaginary component of the complex viscosity is scaled by the Rouse viscosity and plotted as a function of frequency. The effect of the variation in the internal friction parameter is almost negligible in the low frequency regime and is weak in the high frequency regime.

The difference between the approximate model predictions and the exact BD simulation results are most starkly visible in Fig. 8 (d), where the imaginary component of the complex viscosity is scaled by its corresponding value for a Rouse chain and plotted as a function of the scaled frequency. Firstly, the approximate model predicts a low-frequency plateau that is dependent on the internal friction parameter. The simulation results, however, appear to converge on a low-frequency plateau value that is almost independent of the IV parameter. Secondly, the difference between the two predictions is seen to increase with the internal friction parameter.

In addition to the assumptions made in connection

with the calculation of the stress jump, the Dasbach, Manke, and Williams⁶ approximation also relies on a normal-coordinate transformation, using the eigenvectors of the Rouse matrix, which allows the writing of a separate diffusion equation for each of the normal modes, and the subsequent evaluation of the material functions. Based on the comparison of this approximation against exact BD simulations and the GA prediction, it appears that this route for coordinate transformation is justified for longer chains, but might not be prudent for the two-bead case. Furthermore, as explained in detail by Schieber and coworkers³⁹, the evaluation of the stress tensor in the Dasbach, Manke, and Williams⁶ approach relies on approximating an average of the ratio, $\langle QQ/Q^2 \rangle$, by the ratio of averages, $\langle QQ \rangle / \langle Q^2 \rangle$. This could be another probable source of discrepancy between the approximation and the exact BD simulation results observed in Figs. 7 and 8.

A major motivation for the inclusion of internal friction in early theoretical models for polymeric solutions^{32,36,53} was to explain the high-frequency limiting value of the dynamic viscosity, $\eta'(\omega \rightarrow \infty) \equiv \eta'_\infty$, observed in experiments⁵⁴⁻⁵⁶. An improvement to the Rouse/Zimm models was sought since they predict that the dynamic viscosity vanishes in the limit of high frequency, in contrast with experimental observations which in most instances indicate a positive limiting value⁵⁴⁻⁵⁶. Models with internal friction, however, are able to successfully predict this plateau. There do exist systems, however, where the limiting value of the dynamic viscosity in the high frequency limit is *negative*⁵⁷. A detailed experimental investigation of the solvent molecule and polymer segment relaxation dynamics in such systems has been conducted by Lodge and coworkers^{57,58}. They conclude that such negative values of η'_∞ cannot be explained within the existing polymer kinetic theory framework. Suggested modifications to the framework comprise the inclusion of an additional term in the stress tensor expression that accounts for coupling effects between the polymer molecules and the solvent⁵⁹. It is not clear what factors determine when internal friction may be invoked to explain high frequency oscillatory shear data, and when additional physics needs to be considered. This is an important question that awaits theoretical and experimental investigation, but is beyond the scope of the present work.

C. Steady-shear viscometric functions

In Fig. 9, the steady-shear values of the material functions defined in Eq. (12) are scaled by the corresponding values for a Rouse chain and plotted as a function of the characteristic shear rate. Schieber has shown⁴⁰, using the Gaussian approximation for dumbbells, that the zero-shear rate viscometric functions are unaffected by internal viscosity. The simulation data is found to concur with this prediction for all the three material functions. It is found that Ψ_2 is practically zero across the range of

shear rates examined for all the cases.

As observed from Figs. 9 (a) and (d), there is a striking similarity in the steady-shear variation of viscosity between Rouse chains with internal viscosity, and Rouse chains with hydrodynamic interactions^{60,61}, in that there is shear-thinning followed by shear-thickening. For bead-spring-dashpot chains with a fixed number of beads, it is observed that the characteristic shear rate at which the minimum in the viscosity occurs is largely unaffected by the internal friction parameter. At shear rates larger than this critical value, the viscosity is found to increase with an increase in the IV parameter. For Rouse chains with hydrodynamic interactions, not only is the zero-shear-rate viscosity different from the free-draining case, the shear-dependence of viscosity is markedly dependent on the number of beads in the chain⁶⁰: for $N_b < 6$, the Rouse viscosity is lower than the Zimm viscosity, and at large shear rates, where the effect of HI weakens, the viscosity values tend towards the Rouse value, and a shear-thinning is observed, following the Newtonian plateau at low shear rates. For $N_b \geq 6$, however, the Rouse viscosity is greater than the Zimm viscosity, and at higher shear rates, the weakening of hydrodynamic interactions result in an upturn in the viscosity, causing it to approach the Rouse limit. An analogous explanation for the shear-thickening observed in Rouse chains with internal friction does not seem possible, since not only does the internal friction parameter result in a pronounced increase in shear thickening at high shear rates, but the viscosity is also seen to *exceed* the Rouse value, clearly ruling out any weakening of the internal friction effects at high shear rates.

As seen from Figs. 9 (b), the onset of shear-thinning in the first normal stress difference coefficient is pushed to higher shear rates, and the extent of shear-thinning reduced, with an increase in the number of beads at a fixed value of the internal friction parameter. For an internal friction parameter value of $\varphi = 1.0$, and the range of shear rates examined in the present work, there doesn't appear to be a shear-thickening in the first normal stress difference coefficient. BD simulations for Hookean dumbbells with internal friction by Hua and Schieber³⁷ show a similar plateauing in the first normal stress difference coefficient, as seen in the present work. There appears to be a suggestion, but no clear evidence of shear-thickening of Ψ_1 , in their work³⁷.

It is anticipated that a shear-thickening in Ψ_1 would be observed at higher values of the internal friction parameter, as evidenced by Fig. 9 (e), where the effect of the internal friction parameter on the first normal stress difference coefficient is examined for a five-bead chain. At lower values of φ , there is no pronounced shear-thickening in Ψ_1 , but a value of $\varphi = 3.0$ results in the onset of a pronounced shear-thickening at $\lambda_p \dot{\gamma} \approx 100.0$. Furthermore, this critical shear rate for the onset of shear-thickening in Ψ_1 is about an order-of-magnitude larger than that in the case of viscosity.

It appears plausible that the shear-thickening in the

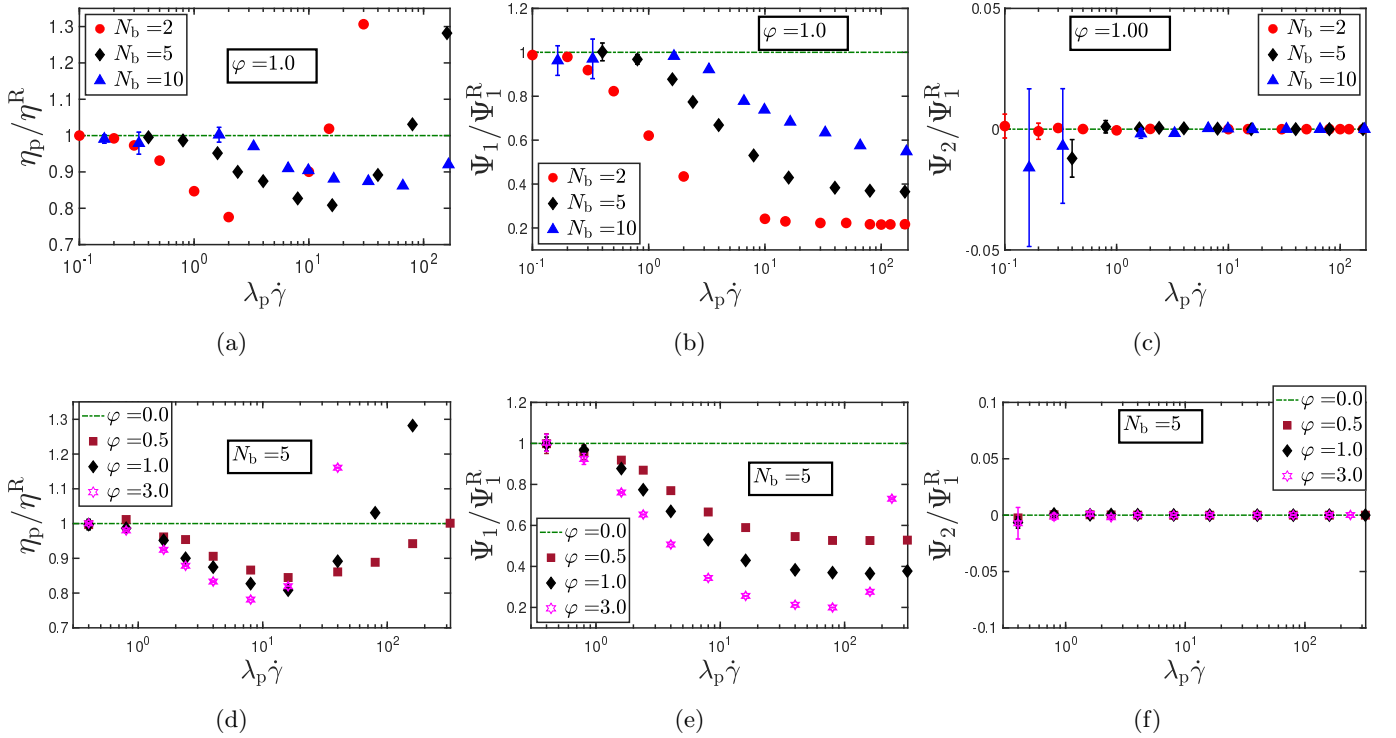


FIG. 9. Steady-shear viscometric functions for bead-spring-dashpot chains with varying (a) number of beads in the chain and (b) values of the internal friction parameter. The horizontal lines in the figures indicate the material functions for a Rouse chain.

viscosity and the first normal stress difference coefficient involves an interplay of internal friction and the number of beads in the chain.

A prevalent notion in the literature^{33,62–64} is that the $\varphi \rightarrow \infty$ corresponds to the rigid-rod limit. This is supported by the following observation. The stress jump for rigid dumbbells with a Gaussian distribution of lengths is given by³⁹ $\eta_{\text{jump,rigid}} = 0.4 n_p k_B T \lambda_H$; while the stress jump for Hookean dumbbells with IV has the following form given by Manke and Williams⁵, $\eta_{\text{jump,IV}} = 0.4 [2\varphi/(1+2\varphi)] n_p k_B T \lambda_H$. Clearly, taking the $\varphi \rightarrow \infty$ limit for Hookean spring-dashpots gives the rigid-rod result. The similarity between the two models, however, ceases here, and their steady-shear viscometric functions look markedly different: while bead-rod-chains are known to display a plateau in viscosity at high shear-rates⁶⁵, preceded by a shear-thinning regime, there is a pronounced increase in shear-thickening as φ is increased for flexible chains with internal friction. Furthermore, while the first normal stress difference coefficient for bead-rod chains shear-thins continuously⁶⁵, chains with IV exhibit a slight shear-thickening at high shear rates, as discussed previously.

A detailed comparison of the rheological properties of FENE dumbbells with IV and rigid dumbbells is given in Ref. 38 where it is concluded that a combination of finite extensibility and a high value of the internal friction parameter ($\varphi \geq 5$) is required to qualitatively mimic the

steady-shear rheological response of rigid-rod models.

IV. CONCLUSIONS

The exact set of stochastic differential equations, and a thermodynamically consistent stress tensor expression for a Rouse chain with fluctuating internal friction has been derived. The BD simulation algorithm for the solution of these equations has been validated by comparison against approximate predictions available in the literature for the stress jump, and material functions in oscillatory and steady simple shear flows have been calculated. Semi-analytical predictions⁶ for the dynamic viscosity are in near-quantitative agreement with the exact simulation results, with the accuracy improving with an increase in the number of beads in the chain. The difference between the predictions and the simulation results are more pronounced for the case of the imaginary component of the complex viscosity. The approximation by Dasbach, Manke, and Williams⁶ fails to capture the frequency dependence of η'' for the dumbbell case observed in exact BD simulations and predicted by the Gaussian approximation⁴⁰.

The approach developed by Williams and coworkers^{5,6}, however, is valid only in the linear viscoelastic regime, and cannot be used to obtain steady-shear viscometric predictions. The Gaussian approximation⁴⁰ solution is

only available for Hookean dumbbells with internal friction, and is unable to predict the shear-thickening in viscosity observed in exact Brownian dynamics simulations.

Bead-spring-dashpot chains exhibit a non-monotonous variation in the viscosity with respect to the shear rate, with shear-thinning followed by shear-thickening. At a fixed value of the internal friction parameter, the shear-thickening effect is seen to weaken with an increase in the number of beads in the chain. Increasing the internal friction parameter at a fixed value of the number of beads in the chain leads to an increase in shear-thickening. The inclusion of internal friction results in a slight shear-thickening of the first normal stress difference coefficient, with the onset of thickening pushed to lower shear rates with an increase in the internal friction parameter.

The importance of hydrodynamic interactions in describing the dynamics of dilute polymer solutions is well-documented^{38,66}. However HI has not been considered

in the present work, because its inclusion introduces an explicit coupling between all bead-pairs, and the procedure developed here is not applicable for the decoupling of the connector vector velocities. The solution of bead-spring-dashpot chains with hydrodynamic and excluded volume interactions is a subject for future study.

ACKNOWLEDGMENTS

This work was supported by the MonARCH and MASSIVE computer clusters of Monash University, and the SpaceTime-2 computational facility of IIT Bombay. R. C. acknowledges SERB for funding (Project No. MTR/2020/000230 under MATRICS scheme). We also acknowledge the funding and general support received from the IITB-Monash Research Academy.

Appendix A: Implementation of decoupling methodology and derivation of governing Fokker-Planck equation

Consider the quantity

$$C_k = \frac{\mathbf{Q}_k \cdot [\dot{\mathbf{Q}}_k]}{Q_k^2}; \quad k = 1, 2, \dots, N \quad (\text{A1})$$

Upon taking a dot-product on both the sides of Eq. (2) with \mathbf{Q}_k/Q_k^2 , an equation for C_k is obtained as

$$\begin{aligned} C_k = & \left(\frac{\mathbf{Q}_k}{Q_k^2} \right) \cdot \boldsymbol{\kappa} \cdot \mathbf{Q}_k - \left(\frac{k_B T}{\zeta} \right) \left(\frac{\mathbf{Q}_k}{Q_k^2} \right) \cdot \left[-\frac{\partial \ln \Psi}{\partial \mathbf{Q}_{k-1}} + 2 \frac{\partial \ln \Psi}{\partial \mathbf{Q}_k} - \frac{\partial \ln \Psi}{\partial \mathbf{Q}_{k+1}} \right] - \frac{1}{\zeta} \left(\frac{\mathbf{Q}_k}{Q_k^2} \right) \cdot \left[-\frac{\partial \phi}{\partial \mathbf{Q}_{k-1}} + 2 \frac{\partial \phi}{\partial \mathbf{Q}_k} - \frac{\partial \phi}{\partial \mathbf{Q}_{k+1}} \right] \\ & + \left(\frac{K}{\zeta} \right) C_{k-1} L_{k-1} \left(\frac{\mathbf{Q}_{k-1}}{Q_k} \right) - \left(\frac{2K}{\zeta} \right) C_k + \left(\frac{K}{\zeta} \right) C_{k+1} L_k \left(\frac{\mathbf{Q}_{k+1}}{Q_k} \right) \end{aligned} \quad (\text{A2})$$

where

$$L_k \equiv \cos \theta_k = \frac{\mathbf{Q}_k \cdot \mathbf{Q}_{k+1}}{Q_k Q_{k+1}} \quad (\text{A3})$$

Upon grouping together terms containing C_k on the RHS and simplifying, the generating equation is obtained as

$$\begin{aligned} C_k = & \left(\frac{\zeta}{\zeta + 2K} \right) \left(\frac{\mathbf{Q}_k}{Q_k^2} \right) \cdot (\boldsymbol{\kappa} \cdot \mathbf{Q}_k) - \left(\frac{k_B T}{\zeta + 2K} \right) \left(\frac{\mathbf{Q}_k}{Q_k^2} \right) \cdot \left[-\frac{\partial \ln \Psi}{\partial \mathbf{Q}_{k-1}} + 2 \frac{\partial \ln \Psi}{\partial \mathbf{Q}_k} - \frac{\partial \ln \Psi}{\partial \mathbf{Q}_{k+1}} \right] - \left(\frac{1}{\zeta + 2K} \right) \left(\frac{\mathbf{Q}_k}{Q_k^2} \right) \cdot \left[-\frac{\partial \phi}{\partial \mathbf{Q}_{k-1}} + 2 \frac{\partial \phi}{\partial \mathbf{Q}_k} - \frac{\partial \phi}{\partial \mathbf{Q}_{k+1}} \right] \\ & + \left(\frac{K}{\zeta + 2K} \right) \left[C_{k-1} L_{k-1} \left(\frac{\mathbf{Q}_{k-1}}{Q_k} \right) + C_{k+1} L_k \left(\frac{\mathbf{Q}_{k+1}}{Q_k} \right) \right] \end{aligned} \quad (\text{A4})$$

Eq. (A4) is then subjected to the forward and backward substitution schema discussed previously, to obtain a decoupled expression for C_k . In the forward substitution step, the equation for C_k is substituted into that for C_{k+1} , starting

with $k = 1$. The general expression obtained at the end of this step can be shown, by induction, to be

$$\begin{aligned}
C_k (1 - M_k) &= \left(\frac{K}{\zeta + 2K} \right) C_{k+1} L_k \left(\frac{Q_{k+1}}{Q_k} \right) + \left(\frac{\zeta}{\zeta + 2K} \right) \left(\frac{1}{Q_k} \right) \sum_{l=1}^k \mathbf{\Gamma}_l^{(k)} \cdot (\boldsymbol{\kappa} \cdot \mathbf{Q}_l) \\
&+ (1 - \delta_{kN}) \left(\frac{k_B T}{\zeta + 2K} \right) \left(\frac{1}{Q_k} \right) \left(\frac{\mathbf{Q}_k}{Q_k} \right) \cdot \left(\frac{\partial \ln \Psi}{\partial \mathbf{Q}_{k+1}} \right) + (1 - \delta_{kN}) \left(\frac{1}{\zeta + 2K} \right) \left(\frac{1}{Q_k} \right) \left(\frac{\mathbf{Q}_k}{Q_k} \right) \cdot \left(\frac{\partial \phi}{\partial \mathbf{Q}_{k+1}} \right) \\
&- \left(\frac{k_B T}{\zeta + 2K} \right) \left(\frac{1}{Q_k} \right) \sum_{l=1}^k \mathbf{E}_l^{(k)} \cdot \left(\frac{\partial \ln \Psi}{\partial \mathbf{Q}_l} \right) - \left(\frac{1}{\zeta + 2K} \right) \left(\frac{1}{Q_k} \right) \sum_{l=1}^k \mathbf{E}_l^{(k)} \cdot \left(\frac{\partial \phi}{\partial \mathbf{Q}_l} \right)
\end{aligned} \tag{A5}$$

where

$$M_k = \left(\frac{K}{\zeta + 2K} \right)^2 \left(\frac{L_{k-1}^2}{1 - M_{k-1}} \right); \quad \text{with} \quad M_1 = 0, \tag{A6}$$

$$\mathbf{\Gamma}_l^{(k)} = \left(\frac{K}{\zeta + 2K} \right)^{k-l} \left[\prod_{i=l}^{k-1} \left(\frac{1}{1 - M_i} \right) L_i \right] \left(\frac{\mathbf{Q}_l}{Q_l} \right), \tag{A7}$$

and

$$\mathbf{E}_l^{(k)} = 2\mathbf{\Gamma}_l^{(k)} - \mathbf{\Gamma}_{l-1}^{(k)} - \mathbf{\Gamma}_{l+1}^{(k)} \tag{A8}$$

Here, $\mathbf{\Gamma}_l^{(k)}$ is defined only for $0 < l \leq k \leq N$, and is set to zero otherwise. The backward substitution step involves plugging in the equation for C_k into C_{k-1} , starting with $k = N$. The general expression at the end of this step can be shown, by induction, to be

$$\begin{aligned}
C_k L_{k-1} \left(\frac{Q_k}{Q_{k-1}} \right) &= \left(\frac{K}{\zeta + 2K} \right) \left(\frac{1}{1 - P_k} \right) C_{k-1} L_{k-1}^2 + \left(\frac{\zeta}{\zeta + 2K} \right) \left(\frac{1}{Q_{k-1}} \right) \sum_{l=k}^N \tilde{\boldsymbol{\rho}}_l^{(k)} \cdot (\boldsymbol{\kappa} \cdot \mathbf{Q}_l) \\
&+ \left(\frac{k_B T}{\zeta + 2K} \right) \left(\frac{1}{1 - P_k} \right) L_{k-1} \left(\frac{1}{Q_{k-1}} \right) \left(\frac{\mathbf{Q}_k}{Q_k} \right) \cdot \left(\frac{\partial \ln \Psi}{\partial \mathbf{Q}_{k-1}} \right) + \left(\frac{1}{\zeta + 2K} \right) \left(\frac{1}{1 - P_k} \right) L_{k-1} \left(\frac{1}{Q_{k-1}} \right) \left(\frac{\mathbf{Q}_k}{Q_k} \right) \cdot \left(\frac{\partial \phi}{\partial \mathbf{Q}_{k-1}} \right) \\
&- \left(\frac{k_B T}{\zeta + 2K} \right) \left(\frac{1}{Q_{k-1}} \right) \sum_{l=k}^N \tilde{\mathbf{G}}_l^{(k)} \cdot \left(\frac{\partial \ln \Psi}{\partial \mathbf{Q}_l} \right) - \left(\frac{1}{\zeta + 2K} \right) \left(\frac{1}{Q_{k-1}} \right) \sum_{l=k}^N \tilde{\mathbf{G}}_l^{(k)} \cdot \left(\frac{\partial \phi}{\partial \mathbf{Q}_l} \right)
\end{aligned} \tag{A9}$$

where

$$P_k = \left(\frac{K}{\zeta + 2K} \right)^2 \left(\frac{L_k^2}{1 - P_{k+1}} \right); \quad \text{with} \quad P_N = 0, \tag{A10}$$

and

$$\tilde{\boldsymbol{\rho}}_l^{(k)} = \left(\frac{K}{\zeta + 2K} \right)^{l-k} \left[\prod_{i=k}^l \left(\frac{1}{1 - P_i} \right) L_{i-1} \right] \left(\frac{\mathbf{Q}_l}{Q_l} \right) \tag{A11}$$

The vector $\tilde{\mathbf{G}}_l^{(k)}$ appearing in Eq. (A9) is constructed using a slightly elaborate procedure. It is useful to first consider a block Rouse matrix, \mathbf{R} , of size $\Upsilon \times \Upsilon$, where

$\Upsilon = (N - k) + 1$, whose each element is a 3×3 matrix, and has the following structure,

$$\mathbf{R} = \begin{pmatrix} 2\delta & -\delta & \mathbf{0} & \cdots \\ -\delta & 2\delta & -\delta & \mathbf{0} & \cdots \\ \mathbf{0} & -\delta & 2\delta & -\delta & \cdots \\ \vdots & \vdots & \vdots & & \\ \mathbf{0} & \mathbf{0} & \cdots & -\delta & 2\delta \end{pmatrix} \tag{A12}$$

and define the intermediate quantity,

$$\begin{aligned}
\tilde{\mathbf{Y}}_s^{(k)} &= \left(\frac{K}{\zeta + 2K} \right)^{s-1} \left[\prod_{i=k}^{k+s-1} \left(\frac{1}{1 - P_i} \right) L_{i-1} \right] \\
&\times \left(\frac{\mathbf{Q}_{s+k-1}}{Q_{s+k-1}} \right)
\end{aligned} \tag{A13}$$

which is then used to populate a block matrix, $\hat{\Theta}^{(k)}$, of size $\Upsilon \times \Upsilon$ that has the following structure

$$\hat{\Theta}^{(k)} = \begin{pmatrix} \tilde{\mathbf{Y}}_1^{(k)} & \tilde{\mathbf{Y}}_1^{(k)} & \mathbf{0} & \cdots & \\ \tilde{\mathbf{Y}}_2^{(k)} & \tilde{\mathbf{Y}}_2^{(k)} & \tilde{\mathbf{Y}}_2^{(k)} & \mathbf{0} & \cdots \\ \mathbf{0} & \tilde{\mathbf{Y}}_3^{(k)} & \tilde{\mathbf{Y}}_3^{(k)} & \tilde{\mathbf{Y}}_3^{(k)} & \cdots \\ \vdots & \vdots & \vdots & & \\ \mathbf{0} & \mathbf{0} & \cdots & \tilde{\mathbf{Y}}_\Upsilon^{(k)} & \tilde{\mathbf{Y}}_\Upsilon^{(k)} \end{pmatrix} \quad (\text{A14})$$

We next consider the block matrix $\mathbf{Z}^{(k)}$ constructed from \mathbf{R} and $\hat{\Theta}^{(k)}$, such that $\mathbf{Z}^{(k)} = \mathbf{R} \cdot \hat{\Theta}^{(k)}$. Now, $\tilde{\mathbf{G}}_{k+m}^{(k)} = \mathbf{Z}_{m+1, m+1}^{(k)}$, which is the $(m+1)^{\text{th}}$ diagonal element of $\mathbf{Z}^{(k)}$. A change of variable, $k \rightarrow (k+1)$, in Eq. (A9) permits us to write

$$\begin{aligned} C_{k+1} L_k \left(\frac{Q_{k+1}}{Q_k} \right) &= \left(\frac{K}{\zeta + 2K} \right) \left(\frac{1}{1 - P_{k+1}} \right) C_k L_k^2 + \left(\frac{\zeta}{\zeta + 2K} \right) \left(\frac{1}{Q_k} \right) \sum_{l=k+1}^N \tilde{\rho}_l^{(k+1)} \cdot (\boldsymbol{\kappa} \cdot \mathbf{Q}_l) \\ &+ (1 - \delta_{kN}) \left(\frac{1}{1 - P_{k+1}} \right) L_k \left(\frac{1}{Q_k} \right) \left[\left(\frac{k_B T}{\zeta + 2K} \right) \left(\frac{\mathbf{Q}_{k+1}}{Q_{k+1}} \right) \cdot \left(\frac{\partial \ln \Psi}{\partial \mathbf{Q}_k} \right) + \left(\frac{1}{\zeta + 2K} \right) \left(\frac{\mathbf{Q}_{k+1}}{Q_{k+1}} \right) \cdot \left(\frac{\partial \phi}{\partial \mathbf{Q}_k} \right) \right] \\ &- \left(\frac{k_B T}{\zeta + 2K} \right) \left(\frac{1}{Q_k} \right) \sum_{l=k+1}^N \tilde{\mathbf{G}}_l^{(k+1)} \cdot \left(\frac{\partial \ln \Psi}{\partial \mathbf{Q}_k} \right) - \left(\frac{1}{\zeta + 2K} \right) \left(\frac{1}{Q_k} \right) \sum_{l=k+1}^N \tilde{\mathbf{G}}_l^{(k+1)} \cdot \left(\frac{\partial \phi}{\partial \mathbf{Q}_k} \right) \end{aligned} \quad (\text{A15})$$

Lastly, by inserting the backward substitution result, Eq. (A15), into the equation obtained from forward substitution, Eq. (A5), the decoupled expression is obtained as

$$\begin{aligned} C_k (1 - M_k - P_k) &= \left(\frac{\zeta}{\zeta + 2K} \right) \left(\frac{1}{Q_k} \right) \sum_{l=1}^N \hat{\Lambda}_l^{(k)} \cdot (\boldsymbol{\kappa} \cdot \mathbf{Q}_l) \\ &- \left(\frac{1}{Q_k} \right) \left[\left(\frac{k_B T}{\zeta + 2K} \right) \sum_{l=1}^N \hat{\mathbf{J}}_l^{(k)} \cdot \left(\frac{\partial \ln \Psi}{\partial \mathbf{Q}_l} \right) + \left(\frac{1}{\zeta + 2K} \right) \sum_{l=1}^N \hat{\mathbf{J}}_l^{(k)} \cdot \left(\frac{\partial \phi}{\partial \mathbf{Q}_l} \right) \right] \end{aligned} \quad (\text{A16})$$

with

$$\hat{\Lambda}_l^{(k)} = \begin{cases} \mathbf{\Gamma}_l^{(k)}; & l < k \\ \left(\frac{\mathbf{Q}_k}{Q_k} \right); & l = k \\ \left(\frac{K}{\zeta + 2K} \right) \tilde{\rho}_l^{(k+1)}; & l > k \end{cases} \quad (\text{A17})$$

and

$$\hat{\mathbf{J}}_l^{(k)} = \begin{cases} \mathbf{E}_l^{(k)}; & l < k \\ \mathbf{E}_l^{(k)} - (1 - \delta_{kN}) \left(\frac{1}{1 - P_{k+1}} \right) \left(\frac{K}{\zeta + 2K} \right) L_k \left(\frac{\mathbf{Q}_{k+1}}{Q_{k+1}} \right); & l = k \\ (1 - \delta_{kN}) \left[\left(\frac{K}{\zeta + 2K} \right) \tilde{\mathbf{G}}_l^{(k+1)} - \left(\frac{\mathbf{Q}_k}{Q_k} \right) \right]; & l = k + 1 \\ \left(\frac{K}{\zeta + 2K} \right) \tilde{\mathbf{G}}_l^{(k+1)}; & l > (k + 1) \end{cases} \quad (\text{A18})$$

The procedure for the construction of $\tilde{\mathbf{G}}_l^{(k+1)}$ which appears in Eq. (A18) is fairly similar to that described in Eqs. (A12)–(A14) for the construction of $\tilde{\mathbf{G}}_l^{(k)}$, with the only caveat that the size of the block matrices, \mathbf{R} and the $\hat{\Theta}^{(k+1)}$, remain $\Upsilon \times \Upsilon$, where $\Upsilon = (N - k) + 1$. Defining

$$\begin{aligned}\mathbf{\Lambda}_l^{(k)} &= \left(\frac{1}{1 - M_k - P_k} \right) \hat{\mathbf{\Lambda}}_l^{(k)} \\ \mathbf{J}_l^{(k)} &= \left(\frac{1}{1 - M_k - P_k} \right) \hat{\mathbf{J}}_l^{(k)}\end{aligned}\tag{A19}$$

Eq. (A16) may be rewritten as

$$\begin{aligned}C_k &= \left(\frac{1}{1 + 2\varphi} \right) \left(\frac{1}{Q_k} \right) \sum_{l=1}^N \mathbf{\Lambda}_l^{(k)} \cdot (\boldsymbol{\kappa} \cdot \mathbf{Q}_l) - \left(\frac{1}{1 + 2\varphi} \right) \left(\frac{1}{Q_k} \right) \left[\left(\frac{k_B T}{\zeta} \right) \sum_{l=1}^N \mathbf{J}_l^{(k)} \cdot \left(\frac{\partial \ln \Psi}{\partial \mathbf{Q}_l} \right) \right. \\ &\quad \left. + \left(\frac{1}{\zeta} \right) \sum_{l=1}^N \mathbf{J}_l^{(k)} \cdot \left(\frac{\partial \phi}{\partial \mathbf{Q}_l} \right) \right]\end{aligned}\tag{A20}$$

to give the decoupled expression for C_k . Noting that the equation for the momentum-averaged velocity of the j^{th} connector vector in a freely-draining chain is given by

$$[\dot{\mathbf{Q}}_j] = \boldsymbol{\kappa} \cdot \mathbf{Q}_j - \sum_{k=1}^N \mathbf{A}_{jk} \cdot \left(\frac{k_B T}{\zeta} \frac{\partial \ln \Psi}{\partial \mathbf{Q}_k} + \frac{1}{\zeta} \frac{\partial \phi}{\partial \mathbf{Q}_k} \right) - \varphi \sum_{k=1}^N \mathbf{A}_{jk} \cdot \mathbf{Q}_k C_k\tag{A21}$$

and substituting the expression for C_k from Eq. (A20) into Eq. (A21),

$$\begin{aligned}[\dot{\mathbf{Q}}_j] &= \boldsymbol{\kappa} \cdot \mathbf{Q}_j - \sum_{k=1}^N \mathbf{A}_{jk} \cdot \left(\frac{k_B T}{\zeta} \frac{\partial \ln \Psi}{\partial \mathbf{Q}_k} + \frac{1}{\zeta} \frac{\partial \phi}{\partial \mathbf{Q}_k} \right) - \left(\frac{\varphi}{1 + 2\varphi} \right) \sum_{k,l=1}^N \mathbf{A}_{jk} \cdot \left(\frac{\mathbf{Q}_k}{Q_k} \right) \mathbf{\Lambda}_l^{(k)} \cdot (\boldsymbol{\kappa} \cdot \mathbf{Q}_l) \\ &\quad + \left(\frac{k_B T}{\zeta} \right) \left(\frac{\varphi}{1 + 2\varphi} \right) \sum_{k,l=1}^N \mathbf{A}_{jk} \cdot \left(\frac{\mathbf{Q}_k}{Q_k} \right) \mathbf{J}_l^{(k)} \cdot \left(\frac{\partial \ln \Psi}{\partial \mathbf{Q}_l} \right) + \left(\frac{1}{\zeta} \right) \left(\frac{\varphi}{1 + 2\varphi} \right) \sum_{k,l=1}^N \mathbf{A}_{jk} \cdot \left(\frac{\mathbf{Q}_k}{Q_k} \right) \mathbf{J}_l^{(k)} \cdot \left(\frac{\partial \phi}{\partial \mathbf{Q}_l} \right)\end{aligned}\tag{A22}$$

The dashed and dotted underlined terms in Eq. (A22) are denoted by the tensors $\boldsymbol{\alpha}_{kl}$ and $\boldsymbol{\mu}_{kl}$, respectively. The following simplifications in notation are introduced before proceeding to the next step:

$$\begin{aligned}\boldsymbol{\alpha}_{kl} &= \left(\frac{\mathbf{Q}_k}{Q_k} \right) \mathbf{\Lambda}_l^{(k)}; \quad \boldsymbol{\mu}_{kl} = \left(\frac{\mathbf{Q}_k}{Q_k} \right) \mathbf{J}_l^{(k)} \\ \mathbf{U}_{jl} &= \sum_{k=1}^N \mathbf{A}_{jk} \cdot \boldsymbol{\alpha}_{kl}; \quad \mathbf{V}_{jl} = \sum_{k=1}^N \mathbf{A}_{jk} \cdot \boldsymbol{\mu}_{kl}\end{aligned}\tag{A23}$$

Using Eqs. (A17) and (A19), an alternate definition for $\boldsymbol{\alpha}_{kl}$ that is more convenient for the construction of the stress tensor expression, may be constructed as,

$$\boldsymbol{\alpha}_{kl} = \chi_l^{(k)} \left(\frac{\mathbf{Q}_k \mathbf{Q}_l}{Q_k Q_l} \right)\tag{A24}$$

where

$$\chi_l^{(k)} = \begin{cases} \left(\frac{1}{1 - M_k - P_k} \right) \left(\frac{K}{\zeta + 2K} \right)^{k-l} \left[\prod_{i=l}^{k-1} \left(\frac{1}{1 - M_i} \right) L_i \right]; & l < k \\ \left(\frac{1}{1 - M_k - P_k} \right); & l = k \\ \left(\frac{1}{1 - M_k - P_k} \right) \left(\frac{K}{\zeta + 2K} \right)^{l-k} \left[\prod_{i=k+1}^l \left(\frac{1}{1 - P_i} \right) L_{i-1} \right]; & l > k \end{cases}\tag{A25}$$

The equation for $[\dot{\mathbf{Q}}_j]$ then becomes

$$[\dot{\mathbf{Q}}_j] = \boldsymbol{\kappa} \cdot \mathbf{Q}_j - \sum_{k=1}^N \mathbf{A}_{jk} \cdot \left(\frac{k_B T}{\zeta} \frac{\partial \ln \Psi}{\partial \mathbf{Q}_k} + \frac{1}{\zeta} \frac{\partial \phi}{\partial \mathbf{Q}_k} \right) - \left(\frac{\varphi}{1+2\varphi} \right) \left[\sum_{l=1}^N \mathbf{U}_{jl} \cdot (\boldsymbol{\kappa} \cdot \mathbf{Q}_l) - \left(\frac{k_B T}{\zeta} \right) \sum_{l=1}^N \mathbf{V}_{jl} \cdot \left(\frac{\partial \ln \Psi}{\partial \mathbf{Q}_l} \right) + \left(\frac{1}{\zeta} \right) \sum_{l=1}^N \mathbf{V}_{jl} \cdot \left(\frac{\partial \phi}{\partial \mathbf{Q}_l} \right) \right] \quad (\text{A26})$$

which is simplified to

$$[\dot{\mathbf{Q}}_j] = \left[\boldsymbol{\kappa} \cdot \mathbf{Q}_j - \left(\frac{\varphi}{1+2\varphi} \right) \sum_{k=1}^N \mathbf{U}_{jk} \cdot (\boldsymbol{\kappa} \cdot \mathbf{Q}_k) \right] - \frac{1}{\zeta} \sum_{k=1}^N \left(\mathbf{A}_{jk} - \frac{\varphi}{1+2\varphi} \mathbf{V}_{jk} \right) \cdot \left(\frac{\partial \phi}{\partial \mathbf{Q}_k} \right) - \frac{k_B T}{\zeta} \sum_{k=1}^N \left(\mathbf{A}_{jk} - \frac{\varphi}{1+2\varphi} \mathbf{V}_{jk} \right) \cdot \left(\frac{\partial \ln \Psi}{\partial \mathbf{Q}_k} \right) \quad (\text{A27})$$

As the next step, the expression for $[\dot{\mathbf{Q}}_j]$ will be substituted into the equation of continuity, recognizing that the homogeneous flow profile allows one to write the continuity equation solely in terms of the relative coordinates, \mathbf{Q}_j . This means that the distribution function $\Psi(\mathbf{r}_c, \mathbf{Q}_1, \mathbf{Q}_2, \dots, \mathbf{Q}_N)$ can be replaced by $\psi(\mathbf{Q}_1, \mathbf{Q}_2, \dots, \mathbf{Q}_N)$, and we have

$$\begin{aligned} \frac{\partial \psi}{\partial t} = & - \sum_{j=1}^N \frac{\partial}{\partial \mathbf{Q}_j} \cdot \{ [\dot{\mathbf{Q}}_j] \psi \} = - \sum_{j=1}^N \frac{\partial}{\partial \mathbf{Q}_j} \cdot \left\{ \left[\boldsymbol{\kappa} \cdot \mathbf{Q}_j - \left(\frac{\varphi}{1+2\varphi} \right) \sum_{k=1}^N \mathbf{U}_{jk} \cdot (\boldsymbol{\kappa} \cdot \mathbf{Q}_k) \right. \right. \\ & \left. \left. - \frac{1}{\zeta} \sum_{k=1}^N \left(\mathbf{A}_{jk} - \frac{\varphi}{1+2\varphi} \mathbf{V}_{jk} \right) \cdot \left(\frac{\partial \phi}{\partial \mathbf{Q}_k} \right) \right] \psi \right\} + \frac{k_B T}{\zeta} \sum_{j,k=1}^N \frac{\partial}{\partial \mathbf{Q}_j} \cdot \left(\mathbf{A}_{jk} - \frac{\varphi}{1+2\varphi} \mathbf{V}_{jk} \right) \cdot \frac{\partial \psi}{\partial \mathbf{Q}_k} \end{aligned} \quad (\text{A28})$$

The last term on the RHS of Eq. (A28) must be processed further, in order to render the Fokker-Planck equation amenable to the Itô interpretation²⁹. Invoking the identity

$$\frac{\partial}{\partial \mathbf{Q}_j} \cdot \boldsymbol{\Xi}_{jl} \cdot \frac{\partial h}{\partial \mathbf{Q}_l} = \frac{\partial}{\partial \mathbf{Q}_j} \frac{\partial}{\partial \mathbf{Q}_l} : [\boldsymbol{\Xi}_{jl}^T h] - \frac{\partial}{\partial \mathbf{Q}_j} \cdot \left[h \frac{\partial}{\partial \mathbf{Q}_l} \cdot \boldsymbol{\Xi}_{jl}^T \right], \quad (\text{A29})$$

where $\boldsymbol{\Xi}_{jl}$ is an arbitrary tensor, and h is a scalar, we may write

$$\begin{aligned} \frac{\partial}{\partial \mathbf{Q}_j} \cdot \left(\mathbf{A}_{jk} - \frac{\varphi}{1+2\varphi} \mathbf{V}_{jk} \right) \cdot \frac{\partial \psi}{\partial \mathbf{Q}_k} = & \frac{\partial}{\partial \mathbf{Q}_j} \frac{\partial}{\partial \mathbf{Q}_k} : \left[\left(\mathbf{A}_{jk} - \frac{\varphi}{1+2\varphi} \mathbf{V}_{jk} \right)^T \psi \right] \\ & - \frac{\partial}{\partial \mathbf{Q}_j} \cdot \left\{ \psi \frac{\partial}{\partial \mathbf{Q}_k} \cdot \left(\mathbf{A}_{jk} - \frac{\varphi}{1+2\varphi} \mathbf{V}_{jk} \right)^T \right\} \end{aligned} \quad (\text{A30})$$

Recognizing that the Rouse matrix, \mathbf{A}_{jk} is composed only of constant values independent of the chain connector vectors, we have $(\partial/\partial \mathbf{Q}_k) \cdot \mathbf{A}_{jk}^T = 0$, and can simplify Eq. (A30) to the form

$$\frac{\partial}{\partial \mathbf{Q}_j} \cdot \left(\mathbf{A}_{jk} - \frac{\varphi}{1+2\varphi} \mathbf{V}_{jk} \right) \cdot \frac{\partial \psi}{\partial \mathbf{Q}_k} = \frac{\partial}{\partial \mathbf{Q}_j} \frac{\partial}{\partial \mathbf{Q}_k} : \left[\left(\mathbf{A}_{jk} - \frac{\varphi}{1+2\varphi} \mathbf{V}_{jk} \right)^T \psi \right] + \left(\frac{\varphi}{1+2\varphi} \right) \frac{\partial}{\partial \mathbf{Q}_j} \cdot \left\{ \psi \frac{\partial}{\partial \mathbf{Q}_k} \cdot \mathbf{V}_{jk}^T \right\},$$

which, upon substitution into Eq. (A28), results in

$$\begin{aligned} \frac{\partial \psi}{\partial t} = & - \sum_{j=1}^N \frac{\partial}{\partial \mathbf{Q}_j} \cdot \left\{ \left[\boldsymbol{\kappa} \cdot \mathbf{Q}_j - \left(\frac{\varphi}{1+2\varphi} \right) \sum_{k=1}^N \mathbf{U}_{jk} \cdot (\boldsymbol{\kappa} \cdot \mathbf{Q}_k) - \frac{1}{\zeta} \sum_{k=1}^N \left(\mathbf{A}_{jk} - \frac{\varphi}{1+2\varphi} \mathbf{V}_{jk} \right) \cdot \left(\frac{\partial \phi}{\partial \mathbf{Q}_k} \right) \right. \right. \\ & \left. \left. - \left(\frac{k_B T}{\zeta} \right) \left(\frac{\varphi}{1+2\varphi} \right) \sum_{k=1}^N \frac{\partial}{\partial \mathbf{Q}_k} \cdot \mathbf{V}_{jk}^T \right] \psi \right\} + \frac{k_B T}{\zeta} \sum_{j,k=1}^N \frac{\partial}{\partial \mathbf{Q}_j} \frac{\partial}{\partial \mathbf{Q}_k} : \left[\left(\mathbf{A}_{jk} - \frac{\varphi}{1+2\varphi} \mathbf{V}_{jk} \right)^T \psi \right] \end{aligned} \quad (\text{A31})$$

Defining

$$\hat{\mathbf{A}}_{jk} = \mathbf{A}_{jk} - \frac{\varphi}{1 + 2\varphi} \mathbf{V}_{jk} \quad (\text{A32})$$

and non-dimensionalizing Eq. (A31) using the length- and time-scales, l_H and λ_H , the dimensionless Fokker-Planck equation may be written as shown in Eq. (4) of Sec. II.

-
- ¹W. Kuhn and H. Kuhn, *Helv. Chim. Acta* **28**, 1533 (1945).
²H. C. Booi and P. H. van Wiechen, *J. Chem. Phys.* **52**, 5056 (1970).
³P.-G. de Gennes, *Scaling Concepts in Polymer Physics* (Cornell University Press, Ithaca, 1979).
⁴C. W. Manke and M. C. Williams, *Macromolecules* **18**, 2045 (1985).
⁵C. W. Manke and M. C. Williams, *J. Rheol.* **31**, 495 (1988).
⁶T. P. Dasbach, C. W. Manke, and M. C. Williams, *J. Phys. Chem.* **96**, 4118 (1992).
⁷L. J. Gerhardt and C. W. Manke, *J. Rheol.* **38**, 1227 (1994).
⁸Y. Murayama, H. Wada, and M. Sano, *Eur. Phys. Lett.* **79**, 58001 (2007).
⁹A. Alexander-Katz, H. Wada, and R. R. Netz, *Phys. Rev. Lett.* **103**, 028102 (2009).
¹⁰J. C. F. Schulz, M. S. Miettinen, and R. R. Netz, *J. Phys. Chem. B* **119**, 4565 (2015).
¹¹R. Kailasham, R. Chakrabarti, and J. R. Prakash, *Phys. Rev. Res.* **2**, 013331 (2020).
¹²D. Vincenzi, *Soft Matter*, (2021).
¹³A. Arbe, M. Monkenbusch, J. Stellbrink, D. Richter, B. Farago, K. Almdal, and R. Faust, *Macromolecules* **34**, 1281 (2001).
¹⁴M. G. Poirier and J. F. Marko, *Phys. Rev. Lett.* **88**, 4 (2002).
¹⁵B. S. Khatrri, M. Kawakami, K. Byrne, D. A. Smith, and T. C. B. McLeish, *Biophys. J.* **92**, 1825 (2007).
¹⁶L. Qiu and S. J. Hagen, *J. Am. Chem. Soc.* **126**, 3398 (2004).
¹⁷A. Soranno, B. Buchli, D. Nettels, R. R. Cheng, S. Müller-Spätth, S. H. Pfeil, A. Hoffmann, E. A. Lipman, D. E. Makarov, and B. Schuler, *Proc. Natl. Acad. Sci. U.S.A.* **109**, 17800 (2012).
¹⁸N. Samanta and R. Chakrabarti, *Chem. Phys. Lett.* **582**, 71 (2013).
¹⁹N. Samanta, J. Ghosh, and R. Chakrabarti, *AIP Adv.* **4**, 067102 (2014).
²⁰N. Samanta and R. Chakrabarti, *Physica A* **450**, 165 (2016).
²¹P. Sashi, D. Ramakrishna, and A. K. Bhuyan, *Biochemistry* **55**, 4595 (2016).
²²A. Soranno, A. Holla, F. Dingfelder, D. Nettels, D. E. Makarov, and B. Schuler, *Proc. Natl. Acad. Sci. U.S.A.* **114**, E1833 (2017).
²³A. Das and D. E. Makarov, *J. Phys. Chem. B* **122**, 9049 (2018).
²⁴D. Mondal, R. Adhikari, and P. Sharma, *Sci. Adv.* **6**, eabb0503 (2020).
²⁵S. Subramanian, H. Golla, K. Divakar, A. Kannan, D. De Sancho, and A. N. Naganathan, *J. Phys. Chem. B* **124**, 8973 (2020).
²⁶C.-H. Liang and M. E. Mackay, *J. Rheol.* **37**, 149 (1993).
²⁷N. V. Orr and T. Sridhar, *J. Non-Newtonian Fluid Mech.* **67**, 77 (1996).
²⁸R. B. Bird, C. F. Curtiss, R. C. Armstrong, and O. Hassager, *Dynamics of Polymeric Liquids - Volume 2 : Kinetic Theory* (John Wiley and Sons, New York, 1987).
²⁹H. C. Öttinger, *Stochastic Processes in Polymeric Fluids* (Springer, Berlin, 1996).
³⁰J. Ravi Prakash, "The kinetic theory of dilute solutions of flexible polymers: Hydrodynamic interaction," in *Advances in the Flow and Rheology of Non-Newtonian Fluids*, Rheology Series, Vol. 8, edited by D. Siginer, D. De Kee, and R. Chhabra (Elsevier, Netherlands, 1999) pp. 467–517, 1st ed.
³¹J. D. Schieber and H. C. Öttinger, *J. Rheol.* **38**, 1909 (1994).
³²E. R. Bazúa and M. C. Williams, *J. Polym. Sci. Polym. Phys. Ed.* **12**, 825 (1974).
³³C. W. Manke and M. C. Williams, *J. Rheol.* **33**, 949 (1989).
³⁴R. Cerf, *J. Polym. Sci.* **23**, 125 (1957).
³⁵R. Cerf, *J. Chim. Phys.* **66**, 479 (1969).
³⁶A. Peterlin, *J. Polym. Sci. A-2 Polym. Phys.* **5**, 179 (1967).
³⁷C. C. Hua and J. D. Schieber, *J. Non-Newtonian Fluid Mech.* **56**, 307 (1995).
³⁸R. Kailasham, R. Chakrabarti, and J. R. Prakash, *J. Chem. Phys.* **149**, 094903 (2018).
³⁹C. C. Hua, J. D. Schieber, and C. W. Manke, *Rheol. Acta* **35**, 225 (1996).
⁴⁰J. D. Schieber, *J. Rheol.* **37**, 1003 (1993).
⁴¹R. Sureshkumar and A. N. Beris, *J. Rheol.* **39**, 1361 (1995).
⁴²M. Fixman, *J. Chem. Phys.* **89**, 2442 (1988).
⁴³B. S. Khatrri and T. C. B. McLeish, *Macromolecules* **40**, 6770 (2007).
⁴⁴R. R. Cheng, A. T. Hawk, and D. E. Makarov, *J. Chem. Phys.* **138**, 074112 (2013).
⁴⁵J. C. F. Schulz, L. Schmidt, R. B. Best, J. Dzubiella, and R. R. Netz, *J. Am. Chem. Soc.* **134**, 6273 (2012).
⁴⁶F. Ameseder, A. Radulescu, O. Holderer, P. Falus, D. Richter, and A. M. Stadler, *J. Phys. Chem. Lett.* **9**, 2469 (2018).
⁴⁷R. Kailasham, R. Chakrabarti, and J. R. Prakash, "How important are fluctuations in the treatment of internal friction?" (manuscript under preparation).
⁴⁸W. Press, S. Teukolsky, W. Vetterling, and B. Flannery, *Numerical Recipes 3rd Edition: The Art of Scientific Computing* (Cambridge University Press, 2007).
⁴⁹L. E. Wedgewood, *Rheologica Acta* **32**, 405 (1993).
⁵⁰N. J. Wagner and H. C. Öttinger, *J. Rheol.* **41**, 757 (1997).
⁵¹S. A. Pabit, H. Roder, and S. J. Hagen, *Biochemistry* **43**, 12532 (2004).
⁵²S. J. Hagen, *Curr. Protein Pept. Sci.* **11**, 385 (2010).
⁵³A. Peterlin and C. Reinhold, *Trans. Soc. Rheol.* **11**, 15 (1967).
⁵⁴J. Lamb and A. J. Matheson, *Proc. Royal Soc. A* **281**, 207 (1964).
⁵⁵W. Philippoff, *Trans. Soc. Rheol.* **8**, 117 (1964).
⁵⁶D. J. Massa, J. L. Schrag, and J. D. Ferry, *Macromolecules* **4**, 210 (1971).
⁵⁷R. L. Morris, S. Amelar, and T. P. Lodge, *J. Chem. Phys.* **89**, 6523 (1988).
⁵⁸T. P. Lodge, *J. Phys. Chem.* **97**, 1480 (1993).
⁵⁹R. B. Bird, *Rheol. Acta* **28**, 457 (1989).
⁶⁰W. Zylka, *J. Chem. Phys.* **94**, 4628 (1991).
⁶¹R. Prabhakar and J. R. Prakash, *J. Rheol.* **50**, 561 (2006).
⁶²C. W. Manke and M. C. Williams, *J. Rheol.* **30**, 19 (1986).
⁶³C. W. Manke and M. C. Williams, *Rheol. Acta* **30**, 316 (1991).
⁶⁴C. W. Manke and M. C. Williams, *Rheol. Acta* **32**, 418 (1993).
⁶⁵D. Petera and M. Muthukumar, *J. Chem. Phys.* **111**, 7614 (1999).
⁶⁶J. R. Prakash, *Curr. Opin. Colloid Interface Sci.* **43**, 63 (2019).

Supplementary Material for: Rouse model with fluctuating internal friction

R. Kailasham,^{1, 2, 3} Rajarshi Chakrabarti,^{2, a)} and J. Ravi Prakash^{3, b)}

¹⁾ IITB-Monash Research Academy, Indian Institute of Technology Bombay, Mumbai, Maharashtra - 400076, India

²⁾ Department of Chemistry, Indian Institute of Technology Bombay, Mumbai, Maharashtra - 400076, India

³⁾ Department of Chemical Engineering, Monash University, Melbourne, VIC 3800, Australia

S1. INTRODUCTION

The main paper outlines a methodology for the derivation of the governing stochastic differential equations (SDE) for a free-draining bead-spring-dashpot chain model for a polymer with internal friction, and presents viscometric functions in steady simple shear and small amplitude oscillatory shear flows. The details corresponding to various aspects of the study have been presented here.

This document is organized as follows. Section S2 presents a route for the conversion of finite continued fractions into ratios of recursive polynomial relations: Secs. S2 A to S2 C present results for polynomial representations of continued fractions, and a list of tensor identities that is useful for the analytical calculation of the divergence terms appearing in the governing stochastic differential equation and the stress tensor expression. In Sec. S2 D, a detailed example of the use of recursive relations is provided. In Sec. S2 E, a comparison between the divergence calculated numerically and using recur-

sive relations is presented. Sec. S2 F discusses the symmetry and positive-definiteness of the diffusion tensor. Lastly, Sec. S3 contains a discussion on the scaling of the computation time of the Brownian dynamics code as a function of the number of beads in the chain.

The connector vectors and associated quantities appearing in this document are in their dimensionless form, with the asterisks omitted for the sake of notational simplicity. Summations are indicated explicitly, and the Einstein summation convention is not followed.

S2. A RECURSIVE ALGORITHM FOR THE CALCULATION OF GRADIENTS OF CONTINUED FRACTIONS

The discrete Euler version of the governing stochastic differential equation for bead-spring-dashpot chains with N_b beads and $N \equiv (N_b - 1)$ springs, and the stress tensor expression, are reproduced here from Sec. II of the main paper

$$\begin{aligned} \tilde{\mathbf{Q}}(t_{n+1}) = & \tilde{\mathbf{Q}}_n + \left[\boldsymbol{\kappa}(t_n) \cdot \tilde{\mathbf{Q}}(t_n) - \left(\frac{\varphi}{1+2\varphi} \right) \boldsymbol{\mathcal{U}}(t_n) \cdot \left(\boldsymbol{\kappa}(t_n) \cdot \tilde{\mathbf{Q}}(t_n) \right) - \frac{1}{4} \boldsymbol{\mathcal{D}}(t_n) \cdot \tilde{\mathbf{F}}^s(t_n) \right. \\ & \left. - \left(\frac{1}{4} \right) \left(\frac{\varphi}{1+2\varphi} \right) \tilde{\mathbf{v}}(t_n) \right] \Delta t_n + \frac{1}{\sqrt{2}} \Delta \tilde{\mathbf{S}}_n \end{aligned} \quad (1)$$

$$\begin{aligned} \frac{\tau_p}{n_p k_B T} = & (N_b - 1) \delta - \left[\left\langle \sum_{k=1}^N \mathbf{Q}_k \mathbf{F}_k^s \right\rangle - \frac{1}{2} \left(\frac{\epsilon}{1+\epsilon} \right) \left\langle \sum_{k,l=1}^N (\mathbf{Q}_k \mathbf{F}_l^s) \cdot \boldsymbol{\mu}_{kl}^T \right\rangle \right] - \frac{1}{2} \left(\frac{\epsilon}{1+\epsilon} \right) \left[\left\langle \sum_{k=1}^N \boldsymbol{\mu}_{kk}^T \right\rangle \right. \\ & \left. + \left\langle \sum_{k,l=1}^N \mathbf{Q}_k \frac{\partial}{\partial \mathbf{Q}_l} \cdot \boldsymbol{\mu}_{kl}^T \right\rangle \right] - \left(\frac{2\epsilon}{1+\epsilon} \right) \boldsymbol{\kappa} : \left\langle \sum_{k,l=1}^N \frac{\chi_l^{(k)} \mathbf{Q}_l \mathbf{Q}_l \mathbf{Q}_k \mathbf{Q}_k}{Q_l Q_k} \right\rangle \end{aligned} \quad (2)$$

where $\epsilon = 2\varphi$, $\tilde{\mathbf{v}} \equiv [\hat{\mathbf{v}}_1, \hat{\mathbf{v}}_2, \dots, \hat{\mathbf{v}}_N]$, with $\hat{\mathbf{v}}_j = \sum_{k=1}^N (\partial/\partial \mathbf{Q}_k) \cdot \mathbf{V}_{jk}^T$. Clearly, Eqs. (1) and (2) require the calculation of the divergences $(\partial/\partial \mathbf{Q}_k) \cdot \mathbf{V}_{jk}^T$ and $(\partial/\partial \mathbf{Q}_l) \cdot \boldsymbol{\mu}_{kl}^T$ for all values of $\{j, k, l\} \in [1, N]$. It is straightforward to evaluate these divergences numeri-

cally, using the central difference approximation scheme for the calculation of gradients. In this section, an analytical route for the calculation of these gradients is presented.

It may be seen that both \mathbf{V}_{jk}^T and $\boldsymbol{\mu}_{kl}^T$ possess essentially the same structure, i.e; they may be written as a sum of n_t tensors, as

$$\mathbf{V}_{jk}^T = \boldsymbol{\pi}_1 + \boldsymbol{\pi}_2 + \dots + \boldsymbol{\pi}_{n_t} \quad (3)$$

^{a)} Electronic mail: rajarshi@chem.iitb.ac.in

^{b)} Electronic mail: ravi.jagadeeshan@monash.edu

where each term on the RHS has the following general structure

$$\pi_q = h(M_q, P_q) \left[\frac{\mathbf{Q}_i \mathbf{Q}_m}{\mathbf{Q}_i \mathbf{Q}_m} \right] \quad (4)$$

where $q \in [1, n_t]$, and $i, m \in [(q-1), (q+1)]$. In general, the quantities M_k and P_k are defined recursively as follows

$$\begin{aligned} M_k &= p \left(\frac{L_{k-1}^2}{1 - M_{k-1}} \right); \quad \text{with } M_1 = 0 \\ P_k &= p \left(\frac{L_k^2}{1 - P_{k+1}} \right); \quad \text{with } P_N = 0 \end{aligned} \quad (5)$$

where

$$p = \left(\frac{K}{\zeta + 2K} \right)^2; \quad L_k \equiv \cos \theta_k = \frac{\mathbf{Q}_k \cdot \mathbf{Q}_{k+1}}{Q_k Q_{k+1}} \quad (6)$$

For any scalar h , and any tensor \mathbf{H} , the divergence of their product obeys the following identity,

$$\nabla \cdot (h\mathbf{H}) = (\nabla h) \cdot \mathbf{H} + h \nabla \cdot \mathbf{H} \quad (7)$$

The evaluation of $(\partial/\partial \mathbf{Q}_k) \cdot \mathbf{V}_{jk}^T$ or $(\partial/\partial \mathbf{Q}_l) \cdot \boldsymbol{\mu}_{kl}^T$ would require knowledge of the gradient of the scalar prefactor, $\partial h/\partial \mathbf{Q}_k$. The difficulty in analytically evaluating this gradient term may be illustrated by considering a specific form of $h(M_q, P_q)$, say, $h \equiv [1 - M_6]^{-1}$, which is encountered in the calculation of $\mathbf{\Gamma}_6^{(7)}$, required for the construction of $\mathbf{\Lambda}_6^{(7)}$, and subsequently that of the elements of the block matrix, \mathbf{U} , as evident from Eqs. (A17), (A19) and (A23) of the main paper. Suppose it is desired to calculate the gradient of h with respect to \mathbf{Q}_3 . We may begin by representing h as

$$h = \frac{1}{1 - M_6} = \frac{1}{1 - \frac{pL_5^2}{1 - \frac{pL_4^2}{1 - \frac{pL_3^2}{1 - \frac{pL_2^2}{1 - pL_1^2}}}}} \quad (8)$$

where only L_2 and L_3 are functions of \mathbf{Q}_3 . Clearly, it is not trivial to apply the quotient-rule to evaluate the gradient of h with respect to \mathbf{Q}_3 . Fortunately, continued fractions of the type indicated in Eq. (8), and finite continued products of such fractions, may be expressed as ratios of polynomials^{1,2}.

Suppose we define

$$I_k = (1 - M_1)(1 - M_2) \dots (1 - M_{k-1})(1 - M_k) \quad (9)$$

It can be shown that

$$I_{k+2} = 1 - pL_1^2 - pL_2^2 - p \left[\sum_{i=3}^{k+1} L_i^2 I_{i-1} \right] \quad (10)$$

Similarly, defining

$$D_k = (1 - P_k)(1 - P_{k+1}) \dots (1 - P_{N-1})(1 - P_N) \quad (11)$$

where N is the number of springs in the chain, it can be shown that

$$D_k = 1 - pL_{N-1}^2 - pL_{N-2}^2 - p \left[\sum_{i=k}^{N-3} L_i^2 D_{i+2} \right] \quad (12)$$

Note that while I_0 is not defined according to Eq. (9), we set $I_0 = I_1 = 1$ for programming convenience. Similarly, we set $D_{N+1} = D_N = 1$ for the same reason.

Using Eqs. (9)–(12), it can be shown that

$$\left[\prod_{i=l}^{k-1} \left(\frac{1}{1 - M_i} \right) \right] = \frac{I_{l-1}}{I_{k-1}}, \quad (13)$$

$$\left[\prod_{i=k+1}^l \left(\frac{1}{1 - P_i} \right) \right] = \frac{D_{l+1}}{D_{k+1}}, \quad (14)$$

$$\frac{1}{1 - M_k} = \frac{I_{k-1}}{I_k}, \quad (15)$$

$$\frac{1}{1 - P_k} = \frac{D_{k+1}}{D_k}, \quad (16)$$

and

$$\frac{1}{1 - M_i - P_k} = \frac{1}{\left(\frac{I_i}{I_{i-1}} \right) + \left(\frac{D_k}{D_{k+1}} \right) - 1} \quad (17)$$

Using the polynomial representations introduced above, we may concisely write

$$\frac{\partial h}{\partial \mathbf{Q}_3} = \frac{\partial}{\partial \mathbf{Q}_3} \left[\frac{1}{1 - M_6} \right] = \frac{\partial}{\partial \mathbf{Q}_3} \left(\frac{I_5}{I_6} \right) \quad (18)$$

The quotient rule may now be applied to the ratio of polynomials given on the RHS of Eq. (18). The next task is to obtain general expressions for the gradients, $\partial I_k/\partial \mathbf{Q}_j$, and $\partial D_k/\partial \mathbf{Q}_j$.

A. Forward continued product

We have seen how a recurrence relation for I_k can be obtained. We now provide an expression for I_k as a polynomial in p . Consider I_k where $1 \leq k \leq N$ is any integer.

The degree, n , of the polynomial in p that expresses I_k

is given by $n = \left\lfloor \frac{k}{2} \right\rfloor$ where $[i]$ represents the greatest integer lesser than or equal to i . We can then write

$$I_k = 1 - p \sum_{i=1}^{k-1} L_i^2 f(1, k+1, i) + p^2 \sum_{i=1}^{k-3} L_i^2 f(2, k-1, i) - p^3 \sum_{i=1}^{k-5} L_i^2 f(3, k-3, i) \dots$$

$$+ (-1)^n p^n \sum_{i=1}^{k-(2n-1)} L_i^2 f(n, [k - (2n-3)], i) \quad (19)$$

where the function $f(m, l, j)$ is defined recursively as follows

$$f(m, l, j) = \sum_{s=j+2}^l L_s^2 f(m-1, l+2, s) \quad (20)$$

with

$$f(1, l, j) = 1 \quad \forall \quad l, j \quad (21)$$

While Eq. (19) provides an expression for I_k as a polynomial in p , for the calculation of $\partial I_k / \partial Q_j$, it is desirable to obtain an expansion for I_k in terms of L_ν^2 . As evident from Eq. (6), only L_j and L_{j-1} depend on Q_j . The calculation of $\partial I_k / \partial Q_j$ would therefore be simplified if an expansion in terms of L_ν^2 is available. This is realized in the following expression,

$$I_k = 1 + \sum_{\nu=1}^{k-1} L_\nu^2 \tilde{q}_\nu^{(k)} \quad (22)$$

with

$$\tilde{q}_\nu^{(k)} = \sum_{\mu=1}^n (-1)^\mu p^\mu \tilde{f}(\mu, [k - (2\mu - 3)], -1; \tilde{\ell}) \quad (23)$$

where $1 \leq \nu < k$; $\tilde{\ell}$ may in general be a set of numbers but $\tilde{\ell} = \{\nu\}$ in Eq. (23), and the function $\tilde{f}(m, l, j; \tilde{\ell})$ is defined recursively as

$$\tilde{f}(m, l, j; \tilde{\ell}) = \sum_{\substack{s=j+2 \\ s \notin \tilde{\Lambda} \\ s > \min(\tilde{\ell})}}^l L_s^2 \tilde{f}(m-1, l+2, s; \tilde{\ell})$$

with

$$\tilde{f}(1, l, j; \tilde{\ell}) = 1 \quad \forall \quad l, j, \tilde{\ell} \quad (24)$$

The set $\tilde{\Lambda}$ is related to $\tilde{\ell}$ as follows. For the general case

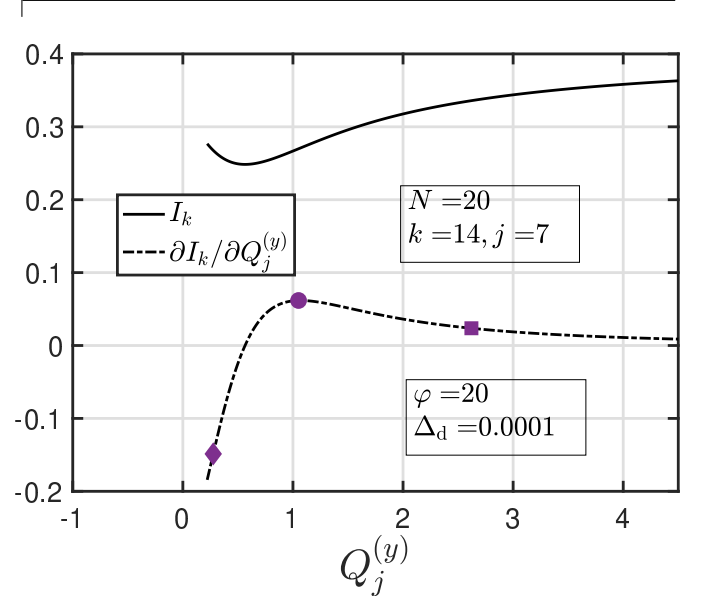


FIG. S1. Plot of I_k [solid line, from Eq. (19)] and its gradient in the y -direction [broken line, from Eq. (29)]. Symbols indicate derivatives calculated using central-difference scheme, with a spatial discretization width of Δ_d .

of $\tilde{\ell} \equiv \{a_1, a_2, a_3, \dots\}$, where the a_i represent arbitrary integers, $\tilde{\Lambda}$ is constructed as

$$\tilde{\Lambda} \equiv \{(a_1 - 1), a_1, (a_1 + 1), (a_2 - 1), a_2, (a_2 + 1), \dots\}$$

For the present case of $\tilde{\ell} = \{\nu\}$, we have $\tilde{\Lambda} = \{\nu-1, \nu, \nu+1\}$. The conditional summation over the index s appearing in the boxed equation above may be understood as follows. For given values of $\{m, l, j; \tilde{\ell}\}$, the index s runs from a lower limit of $j+2$ to an upper limit of l , with two constraints. Firstly, s must not belong to the set $\tilde{\Lambda}$, and secondly, the value of s must be larger than the smallest entry in the set $\tilde{\ell}$. A detailed illustration of the use of the recursive relations, $f(m, l, j)$ and $\tilde{f}(m, l, j; \tilde{\ell})$, has been provided below, in Sec. S2 D.

The next task is to find a general expression for $\frac{\partial \tilde{q}_\nu^{(k)}}{\partial \mathbf{Q}_j}$.
Note that

$$\frac{\partial \tilde{q}_\nu^{(k)}}{\partial \mathbf{Q}_j} = 0; \quad j < \nu + 2 \quad (25)$$

and the following equation holds when $j \geq \nu + 2$,

$$\begin{aligned} \frac{\partial \tilde{q}_\nu^{(k)}}{\partial \mathbf{Q}_j} &= \tilde{\theta}_{j\nu} \left[\sum_{\mu=2}^n (-1)^\mu p^\mu \tilde{f}(\mu-1, [k - (2\mu-5)], -1; \{\nu, j-1\}) \right] \frac{\partial L_{j-1}^2}{\partial \mathbf{Q}_j} \\ &+ \hat{\theta}_{jk} \left[\sum_{\mu=2}^n (-1)^\mu p^\mu \tilde{f}(\mu-1, [k - (2\mu-5)], -1; \{\nu, j\}) \right] \frac{\partial L_j^2}{\partial \mathbf{Q}_j}; \end{aligned} \quad (26)$$

where the underlined terms may be evaluated using Eq. (45) and Eq. (46) given in Sec. S2C, and the indicator functions, $\hat{\theta}_{j\nu}$ and $\hat{\theta}_{jk}$ are defined as

$$\tilde{\theta}_{j\nu} = \begin{cases} 0; & j \leq \nu + 2 \\ 1; & j > \nu + 2 \end{cases} \quad (27)$$

and

$$\hat{\theta}_{jk} = \begin{cases} 0; & j = k \\ 1; & j \neq k \end{cases} \quad (28)$$

which enables us to write

$$\frac{\partial I_k}{\partial \mathbf{Q}_j} = \begin{cases} 0; & j > k \\ \sum_{i=1}^{j-2} L_i^2 \frac{\partial \tilde{q}_i^{(k)}}{\partial \mathbf{Q}_j} + \tilde{q}_{j-1}^{(k)} \frac{\partial L_{j-1}^2}{\partial \mathbf{Q}_j} + \tilde{q}_j^{(k)} \frac{\partial L_j^2}{\partial \mathbf{Q}_j}; & j \leq k \end{cases} \quad (29)$$

In Fig. S1, the derivative of the polynomial I_k , with respect to the y -th component of \mathbf{Q}_j , is plotted for arbitrarily chosen values of $k = 14$, $j = 7$, and the chain length, $N = 20$. There is an excellent agreement between the derivative calculated numerically, and that obtained analytically using Eq. (29).

B. Backward continued product

The backward continued product defined in Eq. (11) may be expressed as a polynomial in p . Consider D_k where $1 \leq k \leq N$ is any integer. The degree, n , of the polynomial in p that expresses D_k is given by $n = \left\lceil \frac{N-k}{2} \right\rceil$ where $\lceil i \rceil$ represents the smallest integer greater than or equal to i . We write

$$\begin{aligned} D_k &= 1 - p \sum_{i=k}^{N-1} L_i^2 g(1, k-2, i) + p^2 \sum_{i=k+2}^{N-1} L_i^2 g(2, k, i) - p^3 \sum_{i=k+4}^{N-1} L_i^2 g(3, k+2, i) \cdots \\ &+ (-1)^n p^n \sum_{i=k+2(n-1)}^{N-1} L_i^2 g(n, [k+2(n-2)], i) \end{aligned} \quad (30)$$

where the function $g(m, l, \gamma)$ is written recursively as

$$g(m, l, \gamma) = \sum_{s=l}^{\gamma-2} L_s^2 g(m-1, l-2, s)$$

with

$$g(1, l, \gamma) = 1 \quad \forall \quad l, \gamma \quad (31)$$

A polynomial expansion for D_k in terms of L_ν may be

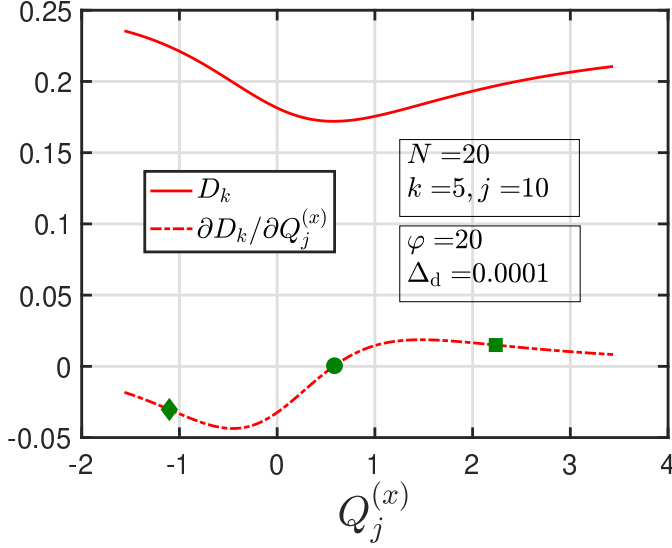


FIG. S2. Plot of D_k [solid line, from Eq. (30)] and its gradient in the x -direction [broken line, from Eq. (37)]. Symbols indicate derivatives calculated using central-difference scheme, with a spatial discretization width of Δ_d .

written as

$$D_k = 1 + \sum_{\nu=k}^{N-1} L_\nu^2 \tilde{w}_\nu^{(k)} \quad (32)$$

where

$$\tilde{w}_\nu^{(k)} = \sum_{\mu=1}^n (-1)^\mu p^\mu \tilde{g}(\mu, [k + 2(\mu - 2)], (N + 1); \tilde{\ell}) \quad (33)$$

where $k \leq \nu < N$, and the function $\tilde{g}(m, l, j; \tilde{\ell})$ is written recursively as follows

$$\tilde{g}(m, l, j; \tilde{\ell}) = \sum_{\substack{s=l \\ s \notin \tilde{\lambda} \\ s > \min(\tilde{\ell})}}^{j-2} L_s^2 \tilde{g}(m-1, l-2, s; \tilde{\ell})$$

with

$$\tilde{g}(1, l, j; \tilde{\ell}) = 1 \quad \forall \quad l, j, \tilde{\ell} \quad (34)$$

In the expansion given by Eq. (33), $\tilde{\ell} = \{\nu\}$, and $\tilde{\lambda} = \{(\nu - 1), \nu, (\nu + 1)\}$.

The next task is to find a general expression for $\frac{\partial \tilde{w}_\nu^{(k)}}{\partial Q_j}$.

Note that

$$\frac{\partial \tilde{w}_\nu^{(k)}}{\partial Q_j} = 0; \quad j < \nu + 2 \quad (35)$$

and the following equation holds when $j \geq \nu + 2$,

$$\begin{aligned} \frac{\partial \tilde{w}_\nu^{(k)}}{\partial Q_j} &= \tilde{\theta}_{j\nu} \left[\sum_{\mu=2}^n (-1)^\mu p^\mu \tilde{g}(\mu - 1, [k + 2(\mu - 3)], (N + 1); \{\nu, j - 1\}) \right] \frac{\partial L_{j-1}^2}{\partial Q_j} \\ &+ \hat{\theta}_{jN} \left[\sum_{\mu=2}^n (-1)^\mu p^\mu \tilde{g}(\mu - 1, [k + 2(\mu - 3)], (N + 1); \{\nu, j\}) \right] \frac{\partial L_j^2}{\partial Q_j}; \end{aligned} \quad (36)$$

which enables us to write

$$\frac{\partial D_k}{\partial Q_j} = \begin{cases} 0; & j < k \\ \sum_{i=k}^{j-2} L_i^2 \frac{\partial \tilde{w}_i^{(k)}}{\partial Q_j} + \tilde{w}_{j-1}^{(k)} \frac{\partial L_{j-1}^2}{\partial Q_j} + \tilde{w}_j^{(k)} \frac{\partial L_j^2}{\partial Q_j}; & j \geq k \end{cases} \quad (37)$$

In Fig. S2, the derivative of the polynomial D_k , with respect to the x -th component of Q_j , is plotted for arbitrarily chosen values of $k = 5$, $j = 10$, and the chain length, $N = 20$. There is an excellent agreement between the derivative calculated numerically, and that obtained analytically using Eq. (37).

C. List of tensor identities

The following identities, useful in the numerical calculation of divergence, are stated without proof:

$$\frac{\partial Q_i^2}{\partial Q_k} = 2Q_i \delta_{ki} \quad (38)$$

$$\frac{\partial}{\partial \mathbf{Q}_k} \left(\frac{\mathbf{Q}_i}{Q_i} \right) = \frac{1}{Q_k} \left[\delta - \frac{\mathbf{Q}_k \mathbf{Q}_k}{Q_k^2} \right] \delta_{ki} \quad (39)$$

$$\frac{\partial}{\partial \mathbf{Q}_k} \cdot \left[\frac{\mathbf{Q}_i \mathbf{Q}_j}{Q_i Q_j} \right] = \left(\frac{1}{Q_i Q_j} \right) \left[\mathbf{Q}_i - \left(\frac{\mathbf{Q}_j \mathbf{Q}_j}{Q_j^2} \right) \cdot \mathbf{Q}_i \right] \delta_{kj} + 2 \left(\frac{\mathbf{Q}_j}{Q_j Q_i} \right) \delta_{ki} \quad (40)$$

$$\begin{aligned} \frac{\partial L_i}{\partial \mathbf{Q}_k} = & \left\{ \left(\frac{1}{Q_i} \right) \left[\left(\frac{\mathbf{Q}_{i+1}}{Q_{i+1}} \right) - L_i \left(\frac{\mathbf{Q}_i}{Q_i} \right) \right] \right\} \delta_{ki} \\ & + \left\{ \left(\frac{1}{Q_{i+1}} \right) \left[\left(\frac{\mathbf{Q}_i}{Q_i} \right) - L_i \left(\frac{\mathbf{Q}_{i+1}}{Q_{i+1}} \right) \right] \right\} \delta_{k,i+1} \end{aligned} \quad (41)$$

Setting $i = (j - 1)$, $k = j$ in Eq. (41),

$$\frac{\partial L_{j-1}}{\partial \mathbf{Q}_j} = \frac{1}{Q_j} \left[\left(\frac{\mathbf{Q}_{j-1}}{Q_{j-1}} \right) - L_{j-1} \left(\frac{\mathbf{Q}_j}{Q_j} \right) \right] \quad (42)$$

Setting $i = k = j$ in Eq. (41),

$$\frac{\partial L_j}{\partial \mathbf{Q}_j} = \frac{1}{Q_j} \left[\left(\frac{\mathbf{Q}_{j+1}}{Q_{j+1}} \right) - L_j \left(\frac{\mathbf{Q}_j}{Q_j} \right) \right] \quad (43)$$

$$\begin{aligned} \frac{\partial L_i^2}{\partial \mathbf{Q}_k} = & \left\{ \left(\frac{2L_i}{Q_i} \right) \left[\left(\frac{\mathbf{Q}_{i+1}}{Q_{i+1}} \right) - L_i \left(\frac{\mathbf{Q}_i}{Q_i} \right) \right] \right\} \delta_{ki} \\ & + \left\{ \left(\frac{2L_i}{Q_{i+1}} \right) \left[\left(\frac{\mathbf{Q}_i}{Q_i} \right) - L_i \left(\frac{\mathbf{Q}_{i+1}}{Q_{i+1}} \right) \right] \right\} \delta_{k,i+1} \end{aligned} \quad (44)$$

Setting $i = (j - 1)$, $k = j$ in Eq. (44) and simplifying,

$$\frac{\partial L_{j-1}^2}{\partial \mathbf{Q}_j} = \frac{2L_{j-1}}{Q_{j-1} Q_j^2} [\mathbf{Q}_j \mathbf{Q}_{j-1} - L_{j-1} Q_{j-1} \mathbf{Q}_j] \quad (45)$$

Setting $i = k = j$ in Eq. (44) and simplifying,

$$\frac{\partial L_j^2}{\partial \mathbf{Q}_j} = \frac{2L_j}{Q_{j+1} Q_j^2} [\mathbf{Q}_j \mathbf{Q}_{j+1} - L_j Q_{j+1} \mathbf{Q}_j] \quad (46)$$

$$\begin{aligned} \frac{\partial}{\partial \mathbf{Q}_k} [L_i L_j] = & \left(\frac{L_i}{Q_j} \right) \left[\left(\frac{\mathbf{Q}_{j+1}}{Q_{j+1}} \right) - L_j \left(\frac{\mathbf{Q}_j}{Q_j} \right) \right] \delta_{kj} + \left(\frac{L_i}{Q_{j+1}} \right) \left[\left(\frac{\mathbf{Q}_j}{Q_j} \right) - L_j \left(\frac{\mathbf{Q}_{j+1}}{Q_{j+1}} \right) \right] \delta_{k,j+1} \\ & + \left(\frac{L_j}{Q_i} \right) \left[\left(\frac{\mathbf{Q}_{i+1}}{Q_{i+1}} \right) - L_i \left(\frac{\mathbf{Q}_i}{Q_i} \right) \right] \delta_{ki} + \left(\frac{L_j}{Q_{i+1}} \right) \left[\left(\frac{\mathbf{Q}_i}{Q_i} \right) - L_i \left(\frac{\mathbf{Q}_{i+1}}{Q_{i+1}} \right) \right] \delta_{k,i+1} \end{aligned} \quad (47)$$

Setting $i = (k - 1)$, $j = k$ in Eq. (47) and simplifying,

$$\frac{\partial}{\partial \mathbf{Q}_k} [L_{k-1} L_k] = \frac{1}{Q_{k-1} Q_k^2 Q_{k+1}} \left\{ Q_{k-1} Q_k L_{k-1} \mathbf{Q}_{k+1} - 2 Q_{k-1} Q_{k+1} L_{k-1} L_k \mathbf{Q}_k + Q_k Q_{k+1} L_k \mathbf{Q}_{k-1} \right\} \quad (48)$$

D. Illustrative example for algorithmic approach to gradient calculation of forward continued product

The application of a recursive-function-based route for the calculation of I_k and $\frac{\partial I_k}{\partial \mathbf{Q}_j}$ will be made clear in this section using an illustrative example, for $k = 8$, $j = 4$ in a chain with $N = 10$ springs. Note that the exact value of N is immaterial for calculations of derivatives involving the forward continued product. The degree, n , of the polynomial in p that expresses I_8 is given by $n = \left\lfloor \frac{8}{2} \right\rfloor = 4$. Using Eq. (19), we have

$$\begin{aligned} I_8 = & 1 - p \sum_{i=1}^{8-1} L_i^2 f(1, [8+1], i) + p^2 \sum_{i=1}^{8-3} L_i^2 f(2, [8-1], i) - p^3 \sum_{i=1}^{8-5} L_i^2 f(3, [8-3], i) + (-1)^4 p^4 \sum_{i=1}^{8-7} L_i^2 f(4, [8-5], i) \\ = & 1 - p \sum_{i=1}^7 L_i^2 f(1, 9, i) + p^2 \sum_{i=1}^5 L_i^2 f(2, 7, i) - p^3 \sum_{i=1}^3 L_i^2 f(3, 5, i) + p^4 \sum_{i=1}^1 L_i^2 f(4, 3, i) \end{aligned} \quad (49)$$

From Eq. (21), the above underlined term is just unity, and Eq. (49) may be simplified as

$$I_8 = 1 - p \sum_{i=1}^7 L_i^2 + p^2 [L_1^2 f(2, 7, 1) + L_2^2 f(2, 7, 2) + L_3^2 f(2, 7, 3) + L_4^2 f(2, 7, 4) + L_5^2 f(2, 7, 5)] \\ - p^3 \left[\underline{L_1^2 f(3, 5, 1)} + L_2^2 f(3, 5, 2) + L_3^2 f(3, 5, 3) \right] + p^4 L_1^2 f(4, 3, 1) \quad (50)$$

The underlined term in Eq. (50) will be evaluated as an example. Using Eq. (20)

$$f(3, 5, 1) = \sum_{s=1+2}^5 L_s^2 f([3-1], [5+2], s) = \sum_{s=3}^5 L_s^2 f(2, 7, s) \\ = L_3^2 f(2, 7, 3) + L_4^2 f(2, 7, 4) + L_5^2 f(2, 7, 5) \\ = L_3^2 \left[\sum_{s=3+2}^7 L_s^2 f([2-1], [7+2], s) \right] + L_4^2 \left[\sum_{s=4+2}^7 L_s^2 f([2-1], [7+2], s) \right] + L_5^2 \left[\sum_{s=5+2}^7 L_s^2 f([2-1], [7+2], s) \right] \\ = L_3^2 [L_5^2 + L_6^2 + L_7^2] + L_4^2 [L_6^2 + L_7^2] + L_5^2 L_7^2 \quad (51)$$

Following a similar procedure, the complete expression for I_8 may be obtained as

$$I_8 = 1 - p (L_1^2 + L_2^2 + L_3^2 + L_4^2 + L_5^2 + L_6^2 + L_7^2) + p^2 [L_1^2 (L_3^2 + L_4^2 + L_5^2 + L_6^2 + L_7^2) + \\ + L_2^2 (L_4^2 + L_5^2 + L_6^2 + L_7^2) + L_3^2 (L_5^2 + L_6^2 + L_7^2) + L_4^2 (L_6^2 + L_7^2) + L_5^2 L_7^2] \\ - p^3 L_1^2 [L_3^2 (L_5^2 + L_6^2 + L_7^2) + L_4^2 (L_6^2 + L_7^2) + L_5^2 L_7^2] - p^3 L_2^2 [L_4^2 (L_6^2 + L_7^2) + L_5^2 L_7^2] - p^3 L_3^2 L_5^2 L_7^2 \\ + p^4 L_1^2 L_3^2 L_5^2 L_7^2 \quad (52)$$

It is now desired to take the gradient of I_8 with respect to \mathbf{Q}_4 . From Eq. (6), it is clear that only L_3 and L_4 are functions of \mathbf{Q}_4 . By grouping together the relevant terms on the RHS of Eq. (52), the expression for $\frac{\partial I_8}{\partial \mathbf{Q}_4}$ may then be written as

$$\frac{\partial I_8}{\partial \mathbf{Q}_4} = \left\{ -p + p^2 (L_1^2 + L_5^2 + L_6^2 + L_7^2) - p^3 L_5^2 L_7^2 - p^3 L_1^2 (L_5^2 + L_6^2 + L_7^2) + p^4 L_1^2 L_5^2 L_7^2 \right\} \frac{\partial L_3^2}{\partial \mathbf{Q}_4} \\ + \left\{ -p + p^2 (L_1^2 + L_2^2 + L_6^2 + L_7^2) - p^3 (L_1^2 + L_2^2) (L_6^2 + L_7^2) \right\} \frac{\partial L_4^2}{\partial \mathbf{Q}_4} \quad (53)$$

where the underlined terms may be evaluated using Eq. (45) and Eq. (46) given in Sec. S2 C. Equation (53) has been obtained using a brute-force approach, by individually examining terms on the RHS of Eq. (52) and retaining the ones that do not vanish when a gradient with respect to \mathbf{Q}_4 is taken. An algorithmic approach for obtaining an expression for $\frac{\partial I_8}{\partial \mathbf{Q}_4}$ is illustrated next. Starting with Eq. (29),

$$\frac{\partial I_8}{\partial \mathbf{Q}_4} = \sum_{i=1}^2 L_i^2 \frac{\partial \tilde{q}_i^{(8)}}{\partial \mathbf{Q}_4} + \tilde{q}_3^{(8)} \frac{\partial L_3^2}{\partial \mathbf{Q}_4} + \tilde{q}_4^{(8)} \frac{\partial L_4^2}{\partial \mathbf{Q}_4} = L_1^2 \frac{\partial \tilde{q}_1^{(8)}}{\partial \mathbf{Q}_4} + L_2^2 \frac{\partial \tilde{q}_2^{(8)}}{\partial \mathbf{Q}_4} + \tilde{q}_3^{(8)} \frac{\partial L_3^2}{\partial \mathbf{Q}_4} + \tilde{q}_4^{(8)} \frac{\partial L_4^2}{\partial \mathbf{Q}_4} \quad (54)$$

The steps for the construction of $\frac{\partial \tilde{q}_1^{(8)}}{\partial \mathbf{Q}_4}$, using Eq. (26), may be written as

$$\begin{aligned} \frac{\partial \tilde{q}_1^{(8)}}{\partial \mathbf{Q}_4} = & \tilde{\theta}_{41} \left[\sum_{\mu=2}^4 (-1)^\mu p^\mu \tilde{f}(\mu-1, [8-(2\mu-5)], -1; \{1, 3\}) \right] \frac{\partial L_3^2}{\partial \mathbf{Q}_4} \\ & + \hat{\theta}_{48} \left[\sum_{\mu=2}^4 (-1)^\mu p^\mu \tilde{f}(\mu-1, [8-(2\mu-5)], -1; \{1, 4\}) \right] \frac{\partial L_4^2}{\partial \mathbf{Q}_4}; \end{aligned} \quad (55)$$

recognizing that $\nu = 1$, $\tilde{\ell} = \{\nu, j-1\} = \{1, 3\}$ for the first term on the RHS of Eq. (55), and $\tilde{\ell} = \{\nu, j\} = \{1, 4\}$ for the second term on the RHS. Upon simplifying Eq. (55) using the indicator functions defined in Eqs. (27) and (28), we obtain

$$\begin{aligned} \frac{\partial \tilde{q}_1^{(8)}}{\partial \mathbf{Q}_4} = & \left[\sum_{\mu=2}^4 (-1)^\mu p^\mu \tilde{f}(\mu-1, [8-(2\mu-5)], -1; \{1, 3\}) \right] \frac{\partial L_3^2}{\partial \mathbf{Q}_4} \\ & + \left[\sum_{\mu=2}^4 (-1)^\mu p^\mu \tilde{f}(\mu-1, [8-(2\mu-5)], -1; \{1, 4\}) \right] \frac{\partial L_4^2}{\partial \mathbf{Q}_4}; \end{aligned} \quad (56)$$

The contents within the square braces, underlined as shown above, will be evaluated explicitly next.

$$\sum_{\mu=2}^4 (-1)^\mu p^\mu \tilde{f}(\mu-1, [8-(2\mu-5)], -1; \{1, 3\}) = p^2 \tilde{f}(1, 9, -1; \{1, 3\}) - p^3 \tilde{f}(2, 7, -1; \{1, 3\}) + p^4 \tilde{f}(3, 5, -1; \{1, 3\}) \quad (57)$$

Now,

$$\tilde{f}(1, 9, -1; \{1, 3\}) = 1 \quad (58)$$

which follows from Eq. (24). The \tilde{f} appearing in the second term on the RHS of Eq. (57) is evaluated as

$$\tilde{f}(2, 7, -1; \{1, 3\}) = \sum_{\substack{s=-1+2 \\ s \notin \tilde{\lambda} \\ s > \min(\{1, 3\})}}^7 L_s^2 \tilde{f}(1, 9, s; \{1, 3\})$$

where $\tilde{\ell} = \{1, 3\}$, and $\tilde{\lambda} \equiv \{(1-1), 1, (1+1), (3-1), 3, (3+1)\} = \{0, 1, 2, 3, 4\}$, with duplicate entries in the set $\tilde{\lambda}$ discarded. We therefore obtain

$$\tilde{f}(2, 7, -1; \{1, 3\}) = \sum_{\substack{s=1 \\ s \notin \{0, 1, 2, 3, 4\} \\ s > 1}}^7 L_s^2 \tilde{f}(1, 9, s; \{1, 3\}) = L_5^2 \underline{\tilde{f}(1, 9, 5; \{1, 3\})} + L_6^2 \underline{\tilde{f}(1, 9, 6; \{1, 3\})} + L_7^2 \underline{\tilde{f}(1, 9, 7; \{1, 3\})}$$

Eq. (24) implies that each of the underlined terms in the above equation is unity, allowing us to write

$$\tilde{f}(2, 7, -1; \{1, 3\}) = L_5^2 + L_6^2 + L_7^2 \quad (59)$$

Similarly,

$$\tilde{f}(3, 5, -1; \{1, 3\}) = \sum_{\substack{s=1 \\ s \notin \{0, 1, 2, 3, 4\} \\ s > 1}}^5 L_s^2 \tilde{f}(2, 7, s; \{1, 3\}) = L_5^2 \tilde{f}(2, 7, 5; \{1, 3\})$$

We then have

$$\tilde{f}(2, 7, 5; \{1, 3\}) = \sum_{\substack{s=7 \\ s \notin \{0, 1, 2, 3, 4\} \\ s > 1}}^7 L_s^2 \tilde{f}(1, 9, s; \{1, 3\}) = L_7^2$$

and may write

$$\tilde{f}(3, 5, -1; \{1, 3\}) = L_5^2 L_7^2 \quad (60)$$

Using Eqs. (58), (59), and (60), Eq. (57) may be rewritten as

$$\sum_{\mu=2}^4 (-1)^\mu p^\mu \tilde{f}(\mu - 1, [8 - (2\mu - 5)], -1; \{1, 3\}) = p^2 - p^3 (L_5^2 + L_6^2 + L_7^2) + p^4 L_5^2 L_7^2 \quad (61)$$

Following along similar lines, the contents of the square braces in the second term on the RHS of Eq. (55) may be evaluated to be

$$\begin{aligned} \sum_{\mu=2}^4 (-1)^\mu p^\mu \tilde{f}(\mu - 1, [8 - (2\mu - 5)], -1; \{1, 4\}) &= p^2 \tilde{f}(1, 9, -1; \{1, 4\}) - p^3 \tilde{f}(2, 7, -1; \{1, 4\}) + p^4 \tilde{f}(3, 5, -1; \{1, 4\}) \\ &= p^2 - p^3 (L_6^2 + L_7^2) \end{aligned} \quad (62)$$

From Eqs. (61) and (62), Eq. (56) may be rewritten as

$$\frac{\partial \tilde{q}_1^{(8)}}{\partial \mathbf{Q}_4} = [p^2 - p^3 (L_5^2 + L_6^2 + L_7^2) + p^4 L_5^2 L_7^2] \frac{\partial L_3^2}{\partial \mathbf{Q}_4} + [p^2 - p^3 (L_6^2 + L_7^2)] \frac{\partial L_4^2}{\partial \mathbf{Q}_4} \quad (63)$$

Following along similar lines, we obtain

$$\frac{\partial \tilde{q}_2^{(8)}}{\partial \mathbf{Q}_4} = [p^2 - p^3 (L_6^2 + L_7^2)] \frac{\partial L_4^2}{\partial \mathbf{Q}_4} \quad (64)$$

The steps for the construction of $\tilde{q}_4^{(8)}$ are given next. Starting from Eq. (23),

$$\begin{aligned} \tilde{q}_4^{(8)} &= \sum_{\mu=1}^4 (-1)^\mu p^\mu \tilde{f}(\mu, [8 - (2\mu - 3)], -1; \{4\}) \\ &= -p \tilde{f}(1, 9, -1; \{4\}) + p^2 \tilde{f}(2, 7, -1; \{4\}) - p^3 \tilde{f}(3, 5, -1; \{4\}) + p^4 \tilde{f}(4, 3, -1; \{4\}) \end{aligned} \quad (65)$$

Now,

$$\tilde{f}(1, 9, -1; \{4\}) = 1 \quad (66)$$

which follows from Eq. (24). The \tilde{f} appearing in the second term on the RHS of Eq. (65) is evaluated as

$$\tilde{f}(2, 7, -1; \{4\}) = \sum_{\substack{s=-1+2 \\ s \notin \tilde{\lambda} \\ s > \min(\{4\})}}^7 L_s^2 \tilde{f}(1, 9, s; \{4\})$$

where $\tilde{\lambda} \equiv \{(4-1), 4, (4+1)\} = \{3, 4, 5\}$. We therefore obtain

$$\tilde{f}(2, 7, -1; \{4\}) = \sum_{\substack{s=1 \\ s \notin \{3, 4, 5\} \\ s > 4}}^7 L_s^2 \tilde{f}(1, 9, s; \{4\}) = L_6^2 \underline{\tilde{f}(1, 9, 6; \{4\})} + L_7^2 \underline{\tilde{f}(1, 9, 7; \{4\})}$$

Eq. (24) implies that each of the underlined terms in the above equation is unity, allowing us to write

$$\tilde{f}(2, 7, -1; \{4\}) = L_6^2 + L_7^2 \quad (67)$$

Processing the terms,

$$\tilde{f}(3, 5, -1; \{4\}) = \sum_{\substack{s=1 \\ s \notin \{3, 4, 5\} \\ s > 4}}^5 L_s^2 \tilde{f}(2, 7, s; \{4\}) = 0; \quad \text{and,} \quad \tilde{f}(4, 3, -1; \{4\}) = \sum_{\substack{s=1 \\ s \notin \{3, 4, 5\} \\ s > 4}}^3 L_s^2 \tilde{f}(3, 5, s; \{4\}) = 0$$

Using Eqs. (66) and (67), Eq. (65) may be rewritten as

$$\tilde{q}_4^{(8)} = -p + p^2 (L_6^2 + L_7^2) \quad (68)$$

Following along similar lines, we obtain

$$\tilde{q}_3^{(8)} = -p + p^2 (L_5^2 + L_6^2 + L_7^2) - p^3 L_5^2 L_7^2 \quad (69)$$

Using Eqs. (63), (64), (68) and (69), Eq. (54) may be rewritten as

$$\begin{aligned} \frac{\partial I_8}{\partial \mathbf{Q}_4} &= L_1^2 \left\{ [p^2 - p^3 (L_5^2 + L_6^2 + L_7^2) + p^4 L_5^2 L_7^2] \frac{\partial L_3^2}{\partial \mathbf{Q}_4} + [p^2 - p^3 (L_6^2 + L_7^2)] \frac{\partial L_4^2}{\partial \mathbf{Q}_4} \right\} \\ &+ L_2^2 \left\{ [p^2 - p^3 (L_6^2 + L_7^2)] \frac{\partial L_4^2}{\partial \mathbf{Q}_4} \right\} + \left\{ -p + p^2 (L_5^2 + L_6^2 + L_7^2) - p^3 L_5^2 L_7^2 \right\} \frac{\partial L_3^2}{\partial \mathbf{Q}_4} + \left\{ -p + p^2 (L_6^2 + L_7^2) \right\} \frac{\partial L_4^2}{\partial \mathbf{Q}_4} \\ &= \left\{ -p + p^2 (L_5^2 + L_6^2 + L_7^2) - p^3 L_5^2 L_7^2 + L_1^2 [p^2 - p^3 (L_5^2 + L_6^2 + L_7^2) + p^4 L_5^2 L_7^2] \right\} \frac{\partial L_3^2}{\partial \mathbf{Q}_4} \\ &+ \left\{ -p + p^2 (L_6^2 + L_7^2) + L_1^2 [p^2 - p^3 (L_6^2 + L_7^2)] + L_2^2 [p^2 - p^3 (L_6^2 + L_7^2)] \right\} \frac{\partial L_4^2}{\partial \mathbf{Q}_4} \end{aligned} \quad (70)$$

which, upon simplification, yields

$$\begin{aligned} \frac{\partial I_8}{\partial \mathbf{Q}_4} &= \left\{ -p + p^2 (L_1^2 + L_5^2 + L_6^2 + L_7^2) - p^3 L_5^2 L_7^2 - p^3 L_1^2 (L_5^2 + L_6^2 + L_7^2) + p^4 L_1^2 L_5^2 L_7^2 \right\} \frac{\partial L_3^2}{\partial \mathbf{Q}_4} \\ &+ \left\{ -p + p^2 (L_1^2 + L_2^2 + L_6^2 + L_7^2) - p^3 (L_1^2 + L_2^2) (L_6^2 + L_7^2) \right\} \frac{\partial L_4^2}{\partial \mathbf{Q}_4} \end{aligned} \quad (71)$$

It is thus observed that Eq. (71), which has been obtained using the recursive-function-based route for the algorithmic calculation of the gradient, is identical to the expression for the gradient written using a brute-force approach, given by Eq. (53).

E. Calculation of divergence terms in SDE and stress tensor expression

As the first step, it is desired to examine the effect of the spatial discretization width, Δ_d , on the accuracy of the numerical calculation of the gradient. As an example, the gradient of $[1/(1 - M_k - P_k)]$, evaluated with respect to the connector vector \mathbf{Q}_j for different values of j, k , and N , using the central-difference approximation [Eq. (19) of the main paper], is compared against the solution obtained using the recursive algorithm detailed in Secs. S2 A- S2 C.

The error in the gradient evaluated using the central-difference approximation is calculated as

$$\% \text{ error} = \frac{|\mathbf{d}_{\text{num}} - \mathbf{d}_{\text{recursive}}|}{|\mathbf{d}_{\text{recursive}}|} \times 100 \quad (72)$$

where $\mathbf{d} \equiv (\partial/\partial \mathbf{Q}_j)[1/(1 - M_k - P_k)]$, and $|\mathbf{d}| = \sqrt{d_x^2 + d_y^2 + d_z^2}$.

In Fig. S3, the variation of this error is plotted as a function of the discretization width, Δ_d , for several test cases. For the data set denoted by empty diamond symbols, the error is seen to decrease nearly monotonically with the decrease in the spatial discretization width. However, for several other data sets, the error varies non-monotonically as the spatial discretization width is changed. Since the minima in the error, where it exists, is observed to occur in the neighbourhood of $\Delta_d = 10^{-5}$, this value of the discretization width has been used in all our calculations. It is noted that the time required for the numerical calculation of the gradient is practically independent of the discretization width.

In Fig. S4, the error in the calculation of divergence terms, which appear in the governing stochastic differential equation and the stress tensor expression, is plotted as a function of the chain length. The error is calculated as

$$\% \text{ error} = \frac{|\mathbf{z}_{\text{num}} - \mathbf{z}_{\text{recursive}}|}{|\mathbf{z}_{\text{recursive}}|} \times 100 \quad (73)$$

where $\mathbf{z} \equiv (\partial/\partial \mathbf{Q}_k) \cdot \mathbf{V}_{jk}^T$ or $(\partial/\partial \mathbf{Q}_l) \cdot \boldsymbol{\mu}_{kl}^T$, and various values of j, k , and l have been considered. The error in all the cases is seen to be $\sim 10^{-7}\%$.

In Fig. S5, the execution time needed for calculating the divergence is plotted as a function of chain length. At lower values of the chain length, the execution times using the two approaches are comparable. With the increase in chain length, however, the time needed for recursive calculation is vastly greater than that for the numerical

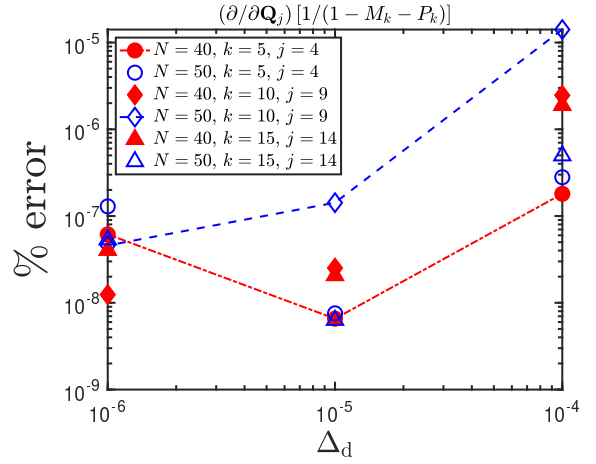


FIG. S3. Variation of error in the calculation of gradient [Eq. (72)], as a function of the spatial discretization width, for two different chain lengths. An internal friction parameter of $\varphi = 200$ is used for all the data points.

route. Furthermore, while the execution time using the direct route is nearly independent of the chain length, the time needed for the recursive route increases precipitously at higher chain lengths, due to the larger number of polynomial evaluations. In view of its faster execution time, and excellent accuracy ($\sim 10^{-7}\%$), the numerical method for divergence calculation has been used in all our simulations.

F. Calculation of square-root of the diffusion tensor

A pre-requisite to the use of the Cholesky decomposition method is that the matrix be positive-definite³. We are not able to prove analytically that the diffusion tensor, \mathcal{D} , appearing in Eq. (6) of the main text is positive-definite. However, we checked for a hundred different random initial configurations of a forty-five spring chain that the eigenvalues of the diffusion matrix are real and positive.

In Fig. S6, the smallest eigenvalue for each sample configuration, and difference between the diffusion matrix and its transpose, are plotted for two different values of the internal friction parameter. The difference is computed as follows: firstly, the diffusion matrix and its transpose are subtracted, to generate a $3N \times 3N$ matrix. This matrix is then unwrapped to give an array, $\hat{\mathbf{d}}$, of $9N^2$ elements. Finally, the 2-norm of this array is computed, and taken to be a numerical measure of the difference between the diffusion matrix and its transpose, as

$$\begin{aligned} \|\mathcal{D}^T - \mathcal{D}\| &\equiv |\hat{\mathbf{d}}| \\ &= \sqrt{(\hat{d}_1)^2 + (\hat{d}_2)^2 + \dots + (\hat{d}_{9N^2})^2} \end{aligned} \quad (74)$$

The difference computed in this manner is $\mathcal{O}(10^{-14})$,

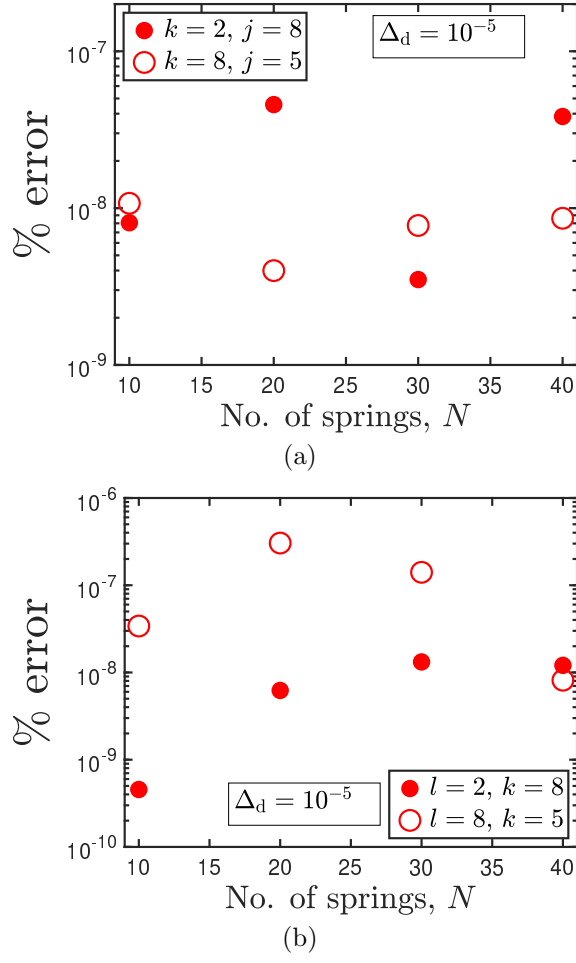


FIG. S4. Error in the calculation of (a) $(\partial/\partial \mathbf{Q}_k) \cdot \mathbf{V}_{jk}^T$ and (b) $(\partial/\partial \mathbf{Q}_l) \cdot \boldsymbol{\mu}_{kl}^T$, as a function of chain length. An internal friction parameter of $\varphi = 200$ is used for all the data points.

meaning that the diffusion matrix may be considered symmetric for all practical purposes.

S3. CPU TIME SCALING

In Fig. S7, the scaling of the execution time as a function of the chain length is presented for a code written using the simple explicit Euler method for solving the SDE. The time taken for simulation of simple Rouse chains scales with an exponent of 1.7 with respect to the chain length, whereas chains with internal friction scale with an exponent of 2.7. Moreover, running simulations on chains with internal friction after dropping the noise term from the governing equation does not seem to significantly affect the execution time, indicating that the calculation of the square root of the diffusion tensor, using Cholesky decomposition, represents only a minor portion of the total workload. Furthermore, the execution time and scaling for chains with internal friction is practically unaffected by the value of the internal friction parameter. The code

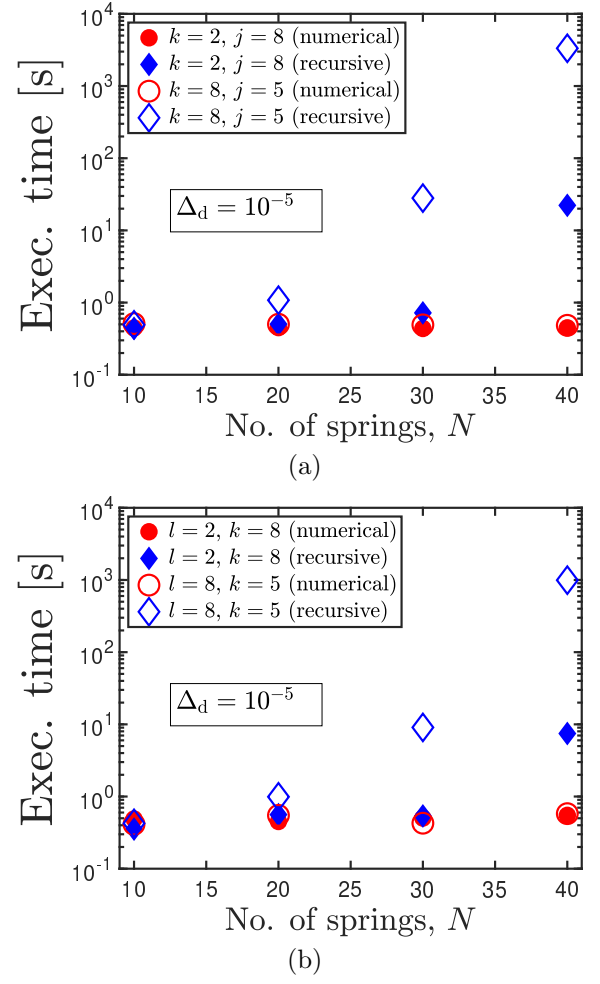


FIG. S5. Execution time, in seconds, for the calculation of (a) $(\partial/\partial \mathbf{Q}_k) \cdot \mathbf{V}_{jk}^T$ and (b) $(\partial/\partial \mathbf{Q}_l) \cdot \boldsymbol{\mu}_{kl}^T$, using two different methods, as a function of chain length. An internal friction parameter of $\varphi = 200$ is used for all the data points. All the runs were executed on MonARCH, the HPC hosted at Monash University, on the same type of processor [16 core Xeon-E5-2667-v3 @ 3.20GHz servers with 100550MB usable memory].

is written in a way that the simulation of chains without internal friction involves neither the construction of the \mathbf{U} and \mathbf{D} matrices, nor the evaluation of the divergence terms or the square-root of the diffusion tensor. In fact, the Rouse case is simulated exactly as given in Eq. (4.4) of Ref. 4, which is a significant simplification over the case with internal friction turned on.

In absolute numbers, the execution time for one trajectory of a ten-bead Rouse chain is 0.07 seconds, whereas that for a ten-bead Rouse chain with internal friction ($\varphi = 1.0$) is 49.6 seconds, representing an increase that is nearly three-orders in magnitude.

¹J. Malila, Appl. Math. E-notes **14**, 13 (2014).

²R. Cretney, Historia Mathematica **41**, 139 (2014).

³W. Press, S. Teukolsky, W. Vetterling, and B. Flannery, *Nu-*

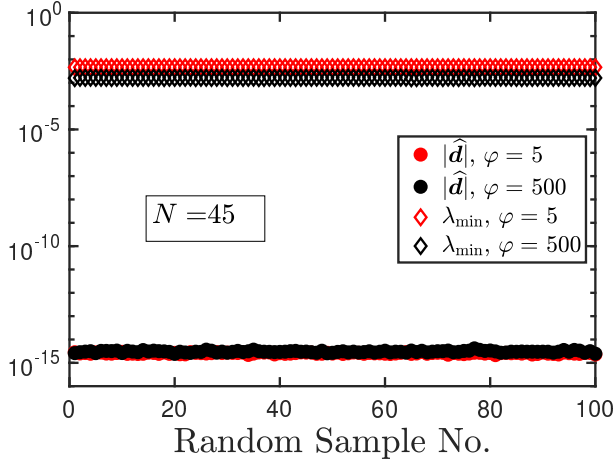


FIG. S6. Test for symmetricity, and smallest eigenvalue of the diffusion tensor, for a hundred randomly chosen initial values of the chain configuration for a forty-five spring chain.

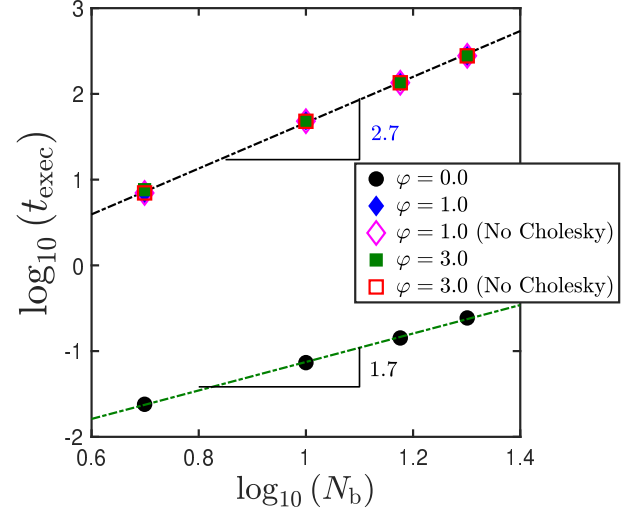


FIG. S7. Scaling of simulation time as a function of number of beads in the chain. Execution time is calculated as an average over one hundred trajectories at each value of N_b . Each trajectory is 100 dimensionless times (λ_H) long. Simulations performed on MonARCH, the HPC hosted at Monash University, with all the runs executed on the same type of processor [16 core Xeon-E5-2667-v3 @ 3.20GHz servers with 100550MB usable memory]. A step size of $\Delta t^* = 10^{-2}$ is used for all the simulation runs.

merical Recipes 3rd Edition: The Art of Scientific Computing (Cambridge University Press, 2007).

⁴H. C. Öttinger, *Stochastic Processes in Polymeric Fluids* (Springer, Berlin, 1996).